Author Manuscript

Author Manuscript

Author Manuscript

Author Manuscript

HHS Public Access

Author manuscript

Cell Rep. Author manuscript; available in PMC 2024 September 26.

Published in final edited form as:

Cell Rep. 2024 August 27; 43(8): 114540. doi:10.1016/j.celrep.2024.114540.

Ca^{2+}-dependent phosphodiesterase 1 regulates the plasticity of striatal spiny projection neuron glutamatergic synapses

Shenyu Zhai[1], **Shintaro Otsuka**[1], **Jian Xu**[1], **Vernon R.J. Clarke**[1], **Tatiana Tkatch**[1], **David Wokosin**[1], **Zhong Xie**[1], **Asami Tanimura**[1,3], **Hitesh K. Agarwal**[2], **Graham C.R. Ellis-Davies**[2], **Anis Contractor**[1], **D. James Surmeier**[1,4,*]

[1]Department of Neuroscience, Feinberg School of Medicine, Northwestern University, Chicago, IL 60611, USA

[2]Department of Neuroscience, Mount Sinai School of Medicine, New York, NY 10029, USA

[3]Present address: Department of Biomedicine, Aarhus University, 8000 Aarhus, Denmark

[4]Lead contact

SUMMARY

Long-term synaptic plasticity at glutamatergic synapses on striatal spiny projection neurons (SPNs) is central to learning goal-directed behaviors and habits. Our studies reveal that SPNs manifest a heterosynaptic, nitric oxide (NO)-dependent form of long-term postsynaptic depression of glutamatergic SPN synapses (NO-LTD) that is preferentially engaged at quiescent synapses. Plasticity is gated by Ca^{2+} entry through $Ca_V1.3$ Ca^{2+} channels and phosphodiesterase 1 (PDE1) activation, which blunts intracellular cyclic guanosine monophosphate (cGMP) and NO signaling. Both experimental and simulation studies suggest that this Ca^{2+}-dependent regulation of PDE1 activity allows for local regulation of dendritic cGMP signaling. In a mouse model of Parkinson disease (PD), NO-LTD is absent because of impaired interneuronal NO release; re-balancing intrastriatal neuromodulatory signaling restores NO release and NO-LTD. Taken together, these studies provide important insights into the mechanisms governing NO-LTD in SPNs and its role in psychomotor disorders such as PD.

In brief

Synaptic plasticity in the brain is generally considered to be dependent on elevated neuronal activity. Zhai et al. describe a heterosynaptic form of postsynaptic, long-term depression of

This is an open access article under the CC BY-NC license (https://creativecommons.org/licenses/by-nc/4.0/).

*Correspondence: j-surmeier@northwestern.edu.

AUTHOR CONTRIBUTIONS

S.Z., D.J.S., S.O., and A.C. designed the experiments. S.Z. performed all electrophysiological and imaging experiments (with the assistance of S.O. and D.W.) and data analysis. S.O., J.X., and A.C. generated the *Cacna1d*$^{G407R/+}$ mice. V.R.J.C. conducted the computational modeling. T.T. and Z.X. performed the biochemical experiments and data analysis. A.T. helped with the viral injection. H.K.A. and G.C.R.E.-D. generated DEAC450-cGMP. S.Z. and D.J.S. prepared the manuscript. All authors approved the final version.

DECLARATION OF INTERESTS

The authors declare no competing interests.

SUPPLEMENTAL INFORMATION

Supplemental information can be found online at https://doi.org/10.1016/j.celrep.2024.114540.

Author Manuscript Author Manuscript Author Manuscript Author Manuscript

glutamatergic synapses in striatal spiny projection neurons that is dependent on inactivity, making it a potential mechanism for “forgetting.”

Graphical abstract

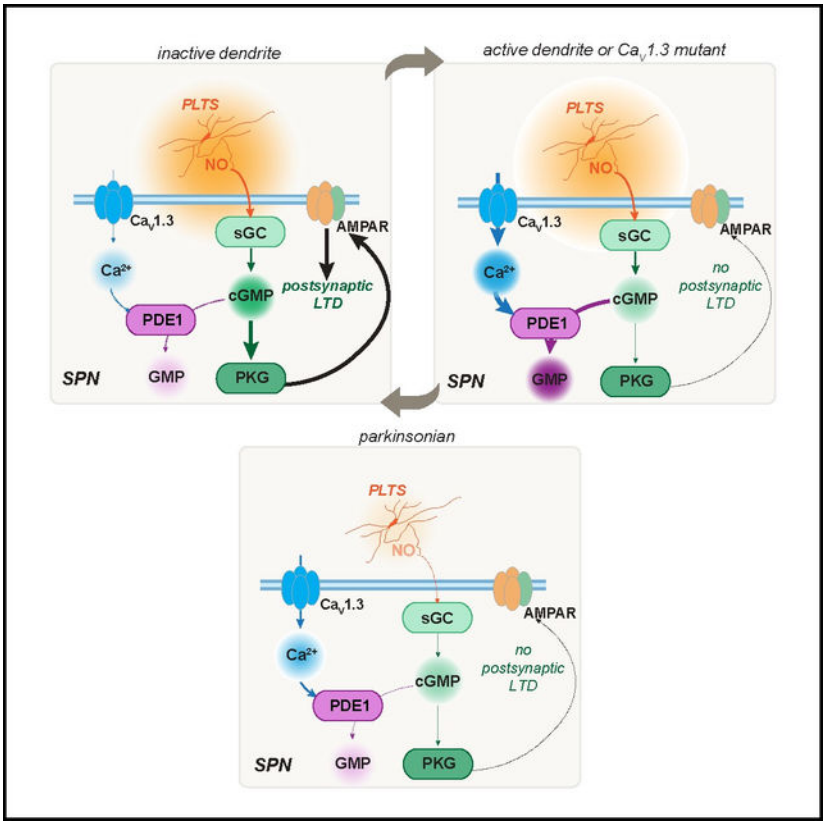

INTRODUCTION

The striatum promotes the selection of context-appropriate actions from a range of possibilities generated by the cortex.[1] This selection process is shaped by reinforcement learning.[2–4] Learning the association between context, action, and outcome manifests itself in the strength of the glutamatergic synapses on striatal spiny projection neurons (SPNs), the principal neurons of the striatum.[2,3,5–9] Several forms of long-term synaptic plasticity have been reported in SPN synapses,[5,6,9,10] but the relationship between them, their differential engagement, and how they might work together to shape learning remains a matter of speculation.

The best-studied form of striatal synaptic plasticity is endocannabinoid-mediated long-term depression (eCB-LTD). This form of plasticity is homosynaptic, postsynaptically induced, and presynaptically expressed.[11–15] It is restricted to corticostriatal glutamatergic synapses and governed by G protein-coupled receptors that are specific to direct pathway SPNs (dSPNs) and indirect pathway SPNs (iSPNs).[16–19] In both types of SPN, eCB-LTD requires

Author Manuscript Author Manuscript Author Manuscript Author Manuscript

the activation of Ca_V1 (L-type) voltage-gated Ca^{2+} channels, primarily those with a low-threshold, $Ca_V1.3$ pore-forming subunit.[14,20–22]

A less studied form of striatal LTD at SPN glutamatergic synapses is heterosynaptic and is expressed postsynaptically. It is triggered by nitric oxide (NO) released by low-threshold spiking interneurons (LTSIs) that express neuronal NO synthase (nNOS).[18,23] In SPNs, NO activates soluble guanylyl cyclase (sGC), which elevates cyclic guanosine monophosphate (cGMP); cGMP signaling triggers the endocytosis of synaptic α-amino-3-hydroxy-5-methyl-4-isoxazolepropionic acid receptors (AMPARs) and LTD. In contrast to eCB-LTD, NO-LTD is inducible at both corticostriatal and thalamostriatal glutamatergic synapses in both types of SPN.[18] However, fundamental questions remain about how this form of synaptic plasticity is regulated and how it contributes to remodeling of striatal circuits in health and disease states such as Parkinson disease (PD).

A regulated step in SPN NO signaling is the degradation of cGMP. This step is controlled by a group of enzymes called phosphodiesterases (PDEs). Two cGMP-degrading PDEs, PDE1B and PDE10A, are highly enriched in the striatum.[24,25] Although both PDEs can degrade cGMP and cyclic adenosine monophosphate (cAMP), their propensity to do so is not the same: PDE1B has a strong preference for cGMP, whereas PDE10A preferentially degrades cAMP.[26,27] Unlike other PDEs, PDE1B is activated by Ca^{2+} and calmodulin,[28,29] making it dependent upon synaptic activity and linking it to both eCB-LTD and long-term potentiation (LTP), which also rely upon an elevation in cytosolic Ca^{2+}.[14,30] However, the cellular determinants of PDE1B activation and its impact on NO-LTD have not been characterized in SPNs.

To help fill this gap, *ex vivo* mouse experiments were used to characterize the mechanisms controlling PDE1 activity and its impact on synaptic plasticity. These studies revealed that dendritic cGMP signaling in SPNs was potently regulated by PDE1B, whose activity was stimulated by Ca^{2+} influx through $Ca_V1.3$ L-type channels. As these channels are prominent in the dendrites and spines of SPNs,[31] this coupling restricted NO-LTD to quiescent dendrites and synapses, which is in sharp contrast to other forms of synaptic plasticity in SPNs. A gain-of-function mutation in the pore-forming subunit of the $Ca_V1.3$ channel led to enhanced dendritic Ca^{2+} entry in SPNs and disruption of NO-LTD. NO-LTD also was disrupted in a mouse model of PD, but in this case, the deficit was attributable to a loss of LTSI NO generation; reversing the PD-induced neuromodulatory imbalance restored NO-LTD in SPNs. Taken together, these studies establish that PDE1 confers inactivity dependence upon heterosynaptic NO-LTD in striatal SPNs, ensuring it is effectively coordinated with other forms of synaptic plasticity.

RESULTS

PDE1 regulated cGMP-dependent LTD in SPNs

Despite the robust expression of PDE1B in the striatum (Figure 1A),[24,25,32–35] its functional role there is still unclear. Given that PDE1B has a high affinity for cGMP (relative to cAMP)[26,36,37] and that cGMP-related signaling molecules are highly expressed in the striatum,[38–41] one possible function of PDE1B is to regulate cGMP signaling in the

Author Manuscript Author Manuscript Author Manuscript Author Manuscript

principal neurons of the striatum, striatal SPNs. As a first step toward assessing this possibility, the expression of PDE1B in iSPNs and dSPNs was determined. Fixed slices from Drd2-EGFP reporter or Drd1-tdTomato mice[42] were immunostained using a PDE1B-specific antibody. PDE1B immunoreactivity was evident in both iSPNs and dSPNs (Figures 1B and S1A).

Previous studies have implicated cGMP signaling in a postsynaptically expressed form of LTD at SPN glutamatergic synapses (NO-LTD).[18,23,43] To determine whether PDE1B regulated NO-LTD, whole-cell patch clamp recordings were made from SPNs in acute brain slices containing dorsolateral striatum (DLS) of Thy1-ChR2 mice, and corticostriatal excitatory postsynaptic currents (EPSCs) were optogenetically evoked with brief blue light-emitting diode (LED) pulses (Figure 1C). Inhibition of PDE1 with a potent and specific inhibitor AF64196 (PDE1i, 0.28 μM)[44] led to a significant time-locked depression of the evoked EPSC amplitude (Figure 1D). As expected from the distribution of PDE1B protein and the heterosynaptic nature of NO signaling, the synaptic depression induced by PDE1i was similar in dSPNs and iSPNs identified using the Drd1-tdTomato or Drd2-EGFP reporter lines (Figures 1E and 1G; $p = 0.1797$). Furthermore, the PDE1i-induced synaptic depression was persistent (or long term), as it was sustained after washing out the inhibitor (Figure S1B). A second, less selective PDE1 inhibitor, 8-methoxymethyl-3-isobutyl-1-methylxanthine (10 μM), also induced a similar depression of corticostriatal EPSCs (Figure S1C).[23] The synaptic depression induced by PDE1i was not dependent upon optical stimulation, as it could also be reproduced when EPSCs were evoked by electrical stimulation (Figure S1D).

To define the role of postsynaptic cGMP signaling in the PDE1i-induced effects, pharmacological tools were used. A principal target of cGMP signaling in SPNs is protein kinase G (PKG).[38] Intracellular application of the competitive PKG inhibitor Rp-8Br-PET-cGMPS (10 μM) blocked PDE1i effects in both dSPNs and iSPNs (Figures 1F and 1G; dSPNs, $p = 0.0022$; iSPNs, $p = 0.0047$). Furthermore, as previously demonstrated for NO-LTD,[18] disrupting AMPAR endocytosis with intracellular infusion of D15 peptide (1 mM)[45] blunted the effects of PDE1i (Figures 1H and 1I; $p = 0.0087$). Also, consistent with a postsynaptic locus of expression, PDE1i-induced LTD was not accompanied by changes in paired pulse ratio (Figure S1E), a hallmark of presynaptic eCB-LTD.[46] Lastly, as with NO-LTD,[18] PDE1i-induced LTD was unaffected by the antagonism of cholinergic signaling through muscarinic or nicotinic receptors (Figure S1F).

To test the possibility that the PDE1i-induced depression of synaptic strength was mediated by allosteric stimulation of PDE2 and a reduction in cAMP levels in SPNs,[47] the impact of PDE1i on corticostriatal synaptic transmission was re-examined in the presence of PDE2 inhibitor Bay 60–7550 at a PDE2-selective concentration (40 nM).[48] Contrary to previous work in cell culture,[47] inhibition of PDE2 in *ex vivo* brain slices did not attenuate the effects of PDE1i on optogenetically evoked EPSCs (oEPSCs) in SPNs (Figure S1G).

To determine whether there were regional differences in PDE1B regulation of synapses, the magnitudes and kinetics of PDE1i-induced LTD at corticostriatal synapses in dorsomedial

Author Manuscript Author Manuscript Author Manuscript Author Manuscript

striatum (DMS) SPNs were compared to those in DLS SPNs. The synaptic depression induced by PDE1i was similar in both striatal regions (Figures 1J and 1K; $p = 0.6504$).

Taken together, these data are consistent with the hypothesis that PDE1B constitutively suppresses NO-LTD at glutamatergic synapses on SPNs. To test the synaptic specificity of the PDE1 regulation, glutamatergic neurons in the thalamic parafascicular nucleus (PFN) were induced to express channelrhodopsin-2 (ChR2) by injecting KH288-grp-Cre mice with a Cre-off ChR2-eYFP (enhanced yellow fluorescent protein) adeno-associated virus (AAV)[49] (Figure 2A). Mice were sacrificed 4–5 weeks after viral injection, *ex vivo* brain slices prepared, and SPNs patch clamped (Figure 2B). Application of PDE1i reliably induced the depression of optogenetically evoked thalamostriatal EPSCs in DLS SPNs (Figures 2C and 2D; corticostriatal vs. thalamostriatal synapses: $p = 0.9636$), demonstrating that glutamatergic synapses arising from both the cortex and thalamus are regulated by PDE1B.

Striatal cholinergic interneurons (ChI) are also strongly excited by NO-induced cGMP signaling.[50–52] However, it is not known whether cGMP in ChIs is regulated by PDE1B. In contrast to SPNs, PDE1B immunoreactivity was not detectable in ChIs identified by fluorescence in striatal sections taken from ChAT-Cre mice crossed with the Ai14 Cre-reporter line (Figure 2E). Moreover, inhibiting PDE1 had no effect on the spontaneous spiking activity of ChIs (Figure S2; $p = 0.4779$). Therefore, the primary function of PDE1 in the striatum is to suppress cGMP signaling and cGMP-dependent LTD at SPN glutamatergic synapses (Figure 2F).

In addition to inducing postsynaptic LTD, cGMP signaling can directly reduce dendritic Ca_V1 Ca^{2+} channel currents in SPNs.[18] Bath application of the non-hydrolyzable cGMP analog 8Br-cGMP (500 μM) diminished the dendritic Ca^{2+} transient evoked by a brief somatic depolarization from −60 to −40 mV (Figures S3A and S3B). To determine whether the inhibition of PDE1 and elevation of *in situ* cGMP signaling would have a similar effect, PDE1i (AF64196, 0.28 μM) was bath applied and the experiment repeated. As predicted, the application of PDE1i significantly diminished the depolarization-induced dendritic Ca^{2+} transient (Figures S3C and S3D), confirming that PDE1 is a crucial regulator of cGMP signaling in SPNs.

PDE1 activity was dependent on $Ca_V1.3$ Ca^{2+} channels

Previous work in cell culture suggests that PDE1 is unique among PDEs in being activated by Ca^{2+}-calmodulin.[36,53] To determine the Ca^{2+} dependence of PDE1 activity in SPNs, neurons were loaded with the high-affinity Ca^{2+} chelator 1,2-bis(*o*-aminophenoxy)ethane-*N,N,N′,N′*-tetraacetic acid (BAPTA, 5 mM) with the patch pipette. BAPTA dialysis significantly blunted the effects of PDE1i application (Figures 3A and 3C). This result suggests that Ca^{2+} chelation diminished PDE1B activity, occluding the effects of PDE1i. As previous work has implicated L-type Ca_V1 Ca^{2+} channels activated by synaptic depolarization in corticostriatal synaptic plasticity,[14,20] a negative allosteric modulator of these channels (isradipine, 2 μM) was bath applied prior to PDE1i application. Doing so blunted the effects of the PDE1i on synaptic transmission (Figures 3B and 3C). Antagonizing *N*-methyl-D-aspartate receptors (NMDARs) with D-AP5 (50 μM) or ryanodine

Author Manuscript Author Manuscript Author Manuscript Author Manuscript

receptors with dantrolene (10 μM) or calcium-permeable AMPARs with 1-naphthylacetyl spermine (NASPM, 20 μM) did not attenuate the PDE1i-mediated suppression of oEPSCs in SPNs (Figures 3C and S4A–S4C). Therefore, in SPNs, PDE1 is primarily activated by L-type Ca^{2+} channels.

The dependence of PDE1 activity on depolarization-activated L-type Ca^{2+} channels led to the prediction that NO/cGMP-evoked LTD might be impaired when membrane voltage is depolarized. *In vivo*, synaptic activity drives the membrane potential of SPNs into a voltage range where $Ca_V1.3$ channels open[31,54] and, in principle, activate PDE1. In agreement with previous work showing the dendritic localization of Ca_V1 channels in SPNs,[22,55] a significant fraction of the dendritic Ca^{2+} signal evoked by stepping up the somatic membrane potential from −70 to −50 mV was inhibited by bath application of isradipine (1 μM) (Figures 3D, 3E, and S4D; $p = 0.0004$). To test the possibility that NO-cGMP-mediated synaptic plasticity would be attenuated by membrane depolarization via Ca_V1 channel-mediated activation of PDE1, the NO donor *S*-nitroso-*N*-acetyl-penicillamine (SNAP) was used. When the somatic membrane potential was held at at −50 mV, the LTD induced by SNAP application (100 μM, 10 min) was attenuated (Figures 3F and 3G).[18,23] However, it was efficiently rescued by isradipine (Figures 3F and 3G; $p = 0.041$), consistent with the hypothesis that Ca^{2+} influx through Ca_V1 channels activates PDE1 and suppresses NO-LTD.

As isradipine and other dihydropyridines do not distinguish channels with a $Ca_V1.2$ or $Ca_V1.3$ pore-forming subunit,[54] the specific role of $Ca_V1.3$ channels was determined by genetic methods. In mice with the *Cacna1d* gene (which codes for the pore-forming subunit of $Ca_V1.3$ channels) floxed (see STAR Methods), an AAV expressing Cre recombinase and tdTomato was injected into the striatum (Figure 3H); 4 weeks later, *ex vivo* brain slices were prepared and tdTomato expression was used to guide patch-clamp recording. In Cre recombinase-expressing SPNs in which *Cacna1d* had been deleted (see Figure S4E), PDE1i application had no effect on corticostriatal synaptic transmission (Figures 3I and 3J). Taken together, these results suggest that Ca^{2+} flux through $Ca_V1.3$ channels stimulates PDE1, blunting cGMP-dependent postsynaptic LTD (Figure 3K).

The gain-of-function G407R mutation in $Ca_V1.3$ channels impaired NO-LTD in SPNs

The involvement of $Ca_V1.3$ Ca^{2+} channels in the regulation of cGMP signaling has implications for our understanding of disease states with striatal determinants. Several missense mutations in the *Cacna1d* gene have been discovered in patients with neurodevelopmental disorders.[56] One that has been associated with autism spectrum disorder (ASD) is a *de novo* glycine- to-arginine mutation at site 407 (G407R).[57] This mutation has been reported to slow channel inactivation in cultured cells, increasing Ca^{2+} flux.[57] To study the cellular consequences of this mutation, a knockin mouse with the G407R mutation in the *Cacna1d* gene was created (Figures S5A–S5C; see STAR Methods) and crossed into the D1-tdTomato reporter line to allow identification of dSPNs. Whole-cell voltage-clamp recording from identified dSPNs was performed in G407R heterozygous ($Cacna1d^{G407R/+}$) and wild-type littermate mice in conjunction with two-photon Ca^{2+} imaging of the dendrites (Figure 4A). Ca^{2+} transients were evoked by depolarizing the soma

Author Manuscript Author Manuscript Author Manuscript Author Manuscript

of SPNs from −60 to −40 mV for 1 s. The contribution of Ca_V1 channels was assessed by bath application of isradipine (2 μM). As predicted from previous work, the dendritic Ca^{2+} transient attributable to Ca_V1 channels was significantly larger in *Cacna1d*$^{G407R/+}$ dSPNs (Figures 4B and 4C; $p = 0.0011$), demonstrating that the G407R mutation increases Ca^{2+} entry through dendritic $Ca_V1.3$ channels.

Next, the functional implications of the mutation were determined by assessing the ability of NO to induce LTD in slices from *Cacna1d*$^{G407R/+}$ mice. In principle, elevated Ca^{2+} entry through $Ca_V1.3$ channels in *Cacna1d*$^{G407R/+}$ SPNs should impair NO-induced LTD by activating PDE1B. To restrict the analysis to corticostriatal synapses, an AAV carrying a ChR2 expression construct was injected into the motor cortex of *Cacna1d*$^{G407R/+}$ mice and wild-type littermates approximately 3 weeks prior to preparing *ex vivo* brain slices (Figure 4D); optogenetic methods were then used to evoke EPSCs in dSPNs. To induce NO-LTD, the NO donor SNAP (5 μM) was applied for 5 min, while SPNs were voltage clamped at −70 mV. This protocol yielded robust LTD of oEPSCs in dSPNs of wild-type siblings (62% ± 1% of baseline at 30–40 min), but only a weak depression of EPSCs in *Cacna*$^{1dG407R/+}$ dSPNs (84% ± 4% of baseline at 30–40 min) (Figures 4E and 4F; $p = 0.0027$). In contrast, bath application of PDE1 inhibitor PDE1i induced a robust LTD in *Cacna1d*$^{G407R/+}$ SPNs (60% ± 2% of baseline at 30–40 min) just as in wild-type littermates (66% ± 1% of baseline at 30–40 min) (Figures 4G and 4H). This suggests that the impairment of NO-LTD in *Cacna1d*$^{G407R/+}$ SPNs was not caused by any changes in the postsynaptic machinery underlying LTD or LTD saturation by ambient NO, but rather was attributable to abnormally high PDE1 activity (Figure 4K). In agreement with this conclusion, striatal PDE1B protein levels were similar in wild types and mutants whether assessed by immunohistochemistry (Figure S5D) or western blot (Figure S5E), arguing that the impairment in NO-LTD was not a consequence of a secondary alteration in SPN PDE1B expression.

$Ca_V1.3$ channels also have been implicated in postsynaptically induced but presynaptically expressed eCB-LTD at corticostriatal synapses in SPNs.[14,15,20,58,59] To determine whether eCB-LTD was altered in *Cacna1d*$^{G407R/+}$ dSPNs, the group I mGluR agonist (*S*)-3,5-dihydroxyphenylglycine (DHPG; 50 μM) was bath applied for 10 min while holding dSPNs at a modestly depolarized potential (−50 mV), a manipulation that elicits eCB release from SPNs and triggers eCB-LTD.[14,15,19] This protocol led to the induction of a robust LTD in dSPNs in both wild-type and *Cacna1d*$^{G407R/+}$ mice (wild type, 61% ± 0.7% of baseline at 31–40 min; *Cacna1d*$^{G407R/+}$, 64% ± 1.3% of baseline at 31–40 min; Figure S6A). This was also the case when eCB-LTD was induced by recording at a less depolarized holding potential (−60 mV) (Figure S6B). To determine whether there was a “ceiling effect” on eCB-LTD, the extracellular Ca^{2+} concentration was lowered to 1.2 mM (from 2 mM). The magnitude of eCB-LTD was reduced by lowering extracellular Ca^{2+} concentration, but to a similar extent in both wild-type and *Cacna1d*$^{G407R/+}$ mice (Figures 4I and 4J; $p = 0.96$). These results suggest that while Ca^{2+} entry through $Ca_V1.3$ channels is necessary to trigger eCB-LTD, the magnitude of the plasticity is controlled by other factors.

Author Manuscript Author Manuscript Author Manuscript Author Manuscript

Dendritic cGMP-evoked LTD was negatively regulated by cytosolic Ca^{2+}

Our results suggest that Ca^{2+} entry through $Ca_V1.3$ channels activates PDE1, suppresses cGMP signaling, and thus prevents the induction of postsynaptic LTD in SPNs. To test this hypothesis, a newly developed, cell-impermeable caged cGMP compound, DEAC450-cGMP,[52] was used to control the spatiotemporal profile of cGMP signaling in SPNs. A patch pipette was used to dialyze SPNs with DEAC450-cGMP (75 μM), and a high concentration of the Ca^{2+} chelator ethylene glycol-bis(β-aminoethyl ether)-*N,N,N′,N′*-tetraacetic acid (EGTA, 5 mM) was used to blunt activation of PDE1 by $Ca_V1.3$ channel opening during synaptic stimulation produced by the electrical stimulation of corticostriatal axons (Figures 5A and 5B). Intracellular uncaging of cGMP triggered a robust postsynaptic LTD (Figure 5C). This LTD was occluded by preincubation with SNAP (Figure S7A). In agreement with a postsynaptic locus of the LTD, the change in EPSC amplitude induced by DEAC450-cGMP uncaging was not accompanied by a change in the paired-pulse ratio (PPR) (Figure 5D). To assess the Ca^{2+} dependence of the LTD induced by intracellular cGMP uncaging, SPNs were dialyzed with a low concentration of EGTA (0.25 mM), enabling Ca^{2+} signaling. In this situation, photolysis of DEAC450-cGMP did not induce LTD (Figure 5C). Dialysis with DEAC450-cGMP and EGTA (5 mM) alone did not affect the corticostriatal EPSC amplitude (Figure S7B).

Dendrites can serve as independent signal processing units, performing local electrical and biochemical integration.[60–62] To determine whether cGMP signaling was localized, DEAC450-cGMP uncaging was restricted to a single dendritic segment, and the effects on synaptic strength were assessed using two-photon glutamate uncaging at that site and on a neighboring dendrite. This was possible because the absorption spectra of DEAC450-cGMP and 4-methoxy-7-nitroindolinyl (MNI)-glutamate do not overlap.[52,63,64] To test the spatial extent of cGMP signaling, SPNs were first filled with DEAC450-cGMP and Alexa Fluor 594 (with 5 mM EGTA) through the patch pipette. Dendritic branches and spines were visualized with two-photon imaging by exciting Alexa Fluor 594 with 1,040-nm light, a wavelength that does not photolyze DEAC450-cGMP or MNI-glutamate. MNI-glutamate was then uncaged with brief pulses of 720 nm light targeted at co-planar dendritic spine heads (Figure 5E). After obtaining uncaging-evoked EPSCs (2pEPSCs), DEAC450-cGMP was uncaged in a short stretch (~35 μm) of dendrite using 473-nm light (200-ms pulses, repeated 5 times with 1-min intervals). Along the dendrite where cGMP had been uncaged, axospinous synapses underwent LTD (Figure 5F). However, on a neighboring dendrite, there was no change in 2pEPSC amplitude (Figure 5F). Dialysis with DEAC450-cGMP alone did not affect the 2pEPSC amplitude, nor did 473-nm light stimulation of dendrites in the absence of DEAC450-cGMP (Figure S7C). Thus, intracellular cGMP signaling, which is tightly regulated by PDE1 activity, produced a dendritically localized, postsynaptic LTD.

A closely related question is how the $Ca_V1.3$ channel dependence of PDE1 limits cGMP signaling when dendrites are more strongly activated and competing forms of plasticity might be induced. Spatiotemporally convergent glutamatergic input to distal SPN dendrites can generate an NMDAR-dependent spike, creating the conditions necessary for LTP induction.[7,65,66] At the dendritic site of spike initiation, the depolarization is presumed to be strong enough to activate voltage-dependent Ca^{2+} channels, including $Ca_V1.3$ channels,[65,67]

Author Manuscript Author Manuscript Author Manuscript Author Manuscript

but how the spike-initiated depolarization changes as a function of distance from this site is unclear. To explore this question, computational simulations were performed using an SPN model in the NEURON simulating environment.[65,67] To evoke a dendritic spike, 18 neighboring glutamatergic synapses were activated at 1-ms intervals in a 15-μm stretch of distal dendrite (Figure 6A). This synaptic stimulation produced a dendritic spike that pushed the local membrane potential to ~−20 mV for about 20 msec; as expected, the dendritic spike had a modest effect on the somatic membrane potential (Figure 6B). A plot of peak membrane potential revealed a strong attenuation of the dendritic spike proximal to its initiation site (Figure 6C). However, in agreement with previous work,[65,68] distal to the site of spike initiation, the peak membrane potential did not decline significantly with distance (Figure 6C). To determine how this profile shaped the opening of $Ca_V1.3$ Ca^{2+} channels (and PDE1 activation), a dendritic heatmap and a plot of $Ca_V1.3$ channel charge density were constructed (Figures 6D–6F). As expected from the non-linear relationship between membrane voltage and channel open probability, the $Ca_V1.3$ channel charge density fell off more rapidly in the proximal dendrite than did voltage; moreover, distal to the stimulation site, channels were strongly activated (Figures 6D–6F). These results suggest that dendritic spikes will engage PDE1 to block cGMP signaling in dendritic regions that are located distally to a dendritic spike, but not in more proximal regions, compartmentalizing NO-cGMP signaling in individual dendritic branches.

Striatal NO signaling was disrupted in a PD model

Conventional forms of synaptic plasticity are lost in striatal SPNs following dopamine (DA) depletion with 6-hydroxydopamine (6-OHDA).[17,69–71] It is not clear whether this deficit extends to NO-LTD. PDE1 inhibition failed to induce synaptic depression in SPNs following an ipsilateral 6-OHDA lesion (Figures 7A and 7D). However, SNAP-induced LTD was normal (Figures 7B and 7D).

One possible explanation for the loss of NO-LTD following a 6-OHDA lesion is that DA depletion disrupts LTSI NO generation. The activity of LTSIs, and presumably their ability to generate NO, is modulated by both activation of D1-type DA receptors and muscarinic acetylcholine receptors (mAChRs).[51,72,73] As DA depletion results in elevated striatal ACh signaling,[49,74,75] the “imbalance” between these modulators could compromise the ability of LTSIs to generate NO. To test this hypothesis, the impact of PDE1 inhibition on synaptic transmission in iSPNs from 6-OHDA-lesioned mice was reexamined after “re-balancing” neuromodulator tone by bath application of the D1-type agonist SKF 81297 (10 μM) and mAChR antagonist scopolamine (10 μM). These experiments focused on iSPNs because of the robust D1R expression in dSPNs.[17] Re-balancing DA and ACh signaling restored the ability of PDE1 inhibition to induce LTD in iSPN from 6-OHDA-lesioned mice (Figures 7C and 7D; $p = 0.0141$).

To better understand the effects of neuromodulator rebalancing, patch-clamp recordings were made from LTSIs identified by fluorescence in *ex vivo* brain slices from NPY-EGFP mice.[76] LTSIs were readily distinguished from neurogliaform interneurons by their spontaneous activity and somatodendritic morphology (Figure 7E).[51,73,77] In brain slices from 6-OHDA-lesioned mice, the LTSI firing rate measured in cell-attached recordings was

Author Manuscript Author Manuscript Author Manuscript Author Manuscript

significantly lower than in controls ($p = 0.0282$) (Figure 7F). Bath application of the D1-type agonist SKF 81297 (10 μM) and mAChR antagonist scopolamine (10 μM) normalized the spiking rate of LTSIs from lesioned mice ($p = 0.0312$) (Figure 7G). Taken together, these data suggest that the NO signaling deficit in PD models stems, at least in part, from slowing of LTSI spiking and reduced nNOS activity (Figure 7H).[78]

DISCUSSION

The studies described here revealed that Ca^{2+} influx through depolarization-activated, $Ca_V1.3$ L-type Ca^{2+} channels activates PDE1B, which potently suppresses constitutive NO/cGMP signaling and the induction of postsynaptic LTD at corticostriatal and thalamostriatal glutamatergic synapses on both iSPNs and dSPNs. As a result of this coupling, NO-LTD at glutamatergic synapses is state dependent; that is, it is preferentially induced in dendritic regions that are relatively quiescent, contrasting it with other well-studied forms of activity-dependent synaptic plasticity in SPNs. The $Ca_V1.3$ channel dependence of PDE1B also helps to ensure that cGMP signaling and postsynaptic LTD are compartmentalized and do not compete with other forms of plasticity at glutamatergic synapses. Our studies also showed that a gain-of-function mutation in $Ca_V1.3$ channels linked to ASD attenuates NO-LTD induction in SPNs. Lastly, our work revealed that in an animal model of PD, constitutive NO signaling from LTSIs is disrupted, potentially contributing to a pathological distortion of the functional connectivity of SPNs and motor disability.

Constitutively engaged NO-LTD is prominent in both iSPNs and dSPNs

Previously it was shown that NO released by LTSIs stimulates sGC and cGMP signaling in SPNs, inducing LTD at glutamatergic synapses.[18,23,43] In contrast to presynaptically expressed eCB-LTD, NO-LTD is expressed postsynaptically and mediated by the endocytosis of AMPARs (shown here and also in reference 18). Inhibition of PDE1B induced LTD in both iSPNs and dSPNs. Furthermore, unlike eCB-LTD at SPN glutamatergic synapses, NO-LTD can occur at both corticostriatal and thalamostriatal axospinous synapses. It also was expressed at axoshaft synapses formed by PFN terminals. Thus, essentially all glutamatergic synapses on DLS SPNs are subject to NO-LTD and regulation by PDE1B.

Precisely how cGMP signaling induces AMPAR endocytosis is unclear. Trafficking of AMPARs is regulated by a broad array of post-translational modifications, including phosphorylation, nitrosylation, and interactions with an auxiliary subunit.[79] Previously, NO-LTD in SPNs was postulated to be mediated by PKG, as it was blocked by the PKG inhibitor Rp-8-Br-PET-cGMPS.[18] At cerebellar parallel fiber-Purkinje cell synapses, PKG also plays a key role in postsynaptic LTD induction.[80] Another potential target of cGMP signaling in SPNs is PDE2.[37] PDE2 is stimulated by cGMP but preferentially degrades cAMP.[81] However, at a concentration selective for PDE2 (40 nM),[48] Bay 60–7550 did not affect NO/cGMP-LTD in SPNs, suggesting that it was not mediated by PDE2.[79] NO-LTD in SPNs also differs from NMDAR-induced LTD,[79] as insertion of Ca^{2+}-permeable AMPARs was unnecessary for induction.

Author Manuscript Author Manuscript Author Manuscript Author Manuscript

Another important inference from our studies was that cGMP signaling in SPNs was constitutive, as inhibition of PDE1 induced LTD without any other extrinsic stimulus. Autonomously active LTSIs are the principal source of striatal NO.[77] Although there are no reliable methods for directly monitoring the spatiotemporal profile of NO produced by a single LTSI, the large axonal fields of LTSIs tile the dorsal striatum,[77] suggesting that essentially all SPNs are exposed to a sustained, diffuse stimulation by NO.

Using non-specific PDE inhibitors, a recent paper reported that cGMP signaling in cortical or thalamic terminals increased presynaptic Ca^{2+} influx and glutamate release.[82] In contrast to the striatum,[33,83] the cortex has very low levels of PDE1B expression but robustly expresses PDE1A. The reported cGMP effect on presynaptic release may be regulated by PDE1A. Nevertheless, in our experiments, bath application of a membrane-permeable cGMP analog or an NO donor (SNAP) produced only synaptic depression that was attributable to a post-synaptic mechanism (see also reference 18), suggesting that the dominant effect of cGMP on striatal glutamatergic synapses was depression.

PDE1B activity was controlled by Ca^{2+} entry $Ca_V1.3$ channels

Three observations argue that PDE1B activity in SPNs is preferentially stimulated by Ca^{2+} entry through $Ca_V1.3$ Ca^{2+} channels. First, the ability of PDE1B inhibition to induce LTD was disrupted by inhibiting Ca_V1 channels with the dihydropyridine isradipine. Second, deleting the gene coding for the pore-forming subunit of $Ca_V1.3$ channels (*Cacna1d*) in adult SPNs blocked the ability of PDE1B inhibition to induce LTD in SPNs. Lastly, in mice harboring a gain-of-function mutation in *Cacna1d*,[57] the ability of the NO donor SNAP to induce LTD at corticostriatal synapses was significantly reduced. In contrast, eCB-LTD, which is stimulated by Ca^{2+} flux through $Ca_V1.3$ channels,[14,15,20,58,59] was intact in mutant SPNs.

The potential biological logic of utilizing $Ca_V1.3$ channels to regulate PDE1B activity is 3-fold. First, $Ca_V1.3$ channels are scaffolded by Shank isoforms close to SPN glutamatergic synapses, putting them in close proximity to the site of cGMP-induced plasticity.[84] Second, Ca^{2+} entry through these channels is a positive modulator of eCB generation and presynaptic LTD,[14,15,20,58,59] allowing them to bi-directionally modulate two competing forms of long-term synaptic depression. Third, the gating properties of $Ca_V1.3$ channels allow them to help compartmentalize cGMP signaling via PDE1B. In distal dendrites (>90 μm from soma), spatiotemporally convergent activity at glutamatergic synapses can generate NMDAR-dependent spikes. These regenerative dendritic events create the conditions necessary for the induction of LTP at co-active glutamatergic synapses; this may allow SPNs to form associations between sensory and motor events.[7,65,66] In agreement with previous work,[65] our simulations suggest that these spikes strongly depolarize more distal dendritic regions, but have much less impact on more proximal regions. The sub-threshold voltage dependence of $Ca_V1.3$ channels ensures that PDE1B will be activated—and NO-LTD blocked—in the active dendritic branches, but enabled in dendrites where the membrane potential is below about −60 mV. Intracellular uncaging of cGMP in dendrites produced a very localized LTD. Proximal dendrites of SPNs do not support synaptically triggered spikes, but axon initial segment spikes decrementally propagate into those regions, where they can trigger

Author Manuscript Author Manuscript Author Manuscript Author Manuscript

eCB-LTD or LTP.[17,85] The voltage dependence of $Ca_V1.3$ channels should ensure that constitutive cGMP signaling is blunted when spikes invade these proximal regions. Thus, coupling $Ca_V1.3$ Ca^{2+} channels to PDE1B in SPNs establishes reciprocity between signaling mechanisms controlling different forms of plasticity at glutamatergic synapses.

Dysregulation of NO-cGMP signaling in PD

Disruption of striatal NO-cGMP signaling has been implicated in network dysfunction accompanying PD.[10] Our studies provide new insight into this connection. A key feature of PD is the loss of the striatal dopaminergic innervation[86] and an elevation in striatal cholinergic interneuron signaling.[75,87–90] Both neuromodulators strongly influence LTSIs: DA normally increases their basal spiking rate and promotes NO release,[72,73,91] whereas ChIs inhibit LTSIs.[73] Consequently, the PD state should be accompanied by lower autonomous LTSI spiking rates and reduced NO production. Previous studies showing that 6-OHDA lesions of the dopaminergic system reduce striatal cGMP levels are consistent with this hypothesis.[92,93] Following a similar lesion of the dopaminergic system, basal LTSI activity was significantly depressed, and constitutive NO-mediated suppression of SPN glutamatergic synapses was lost. Importantly, the reduction in LTSI spiking and deficit in constitutive NO/cGMP signaling were reversed in brain slices from 6-OHDA-lesioned mice by pharmacologically re-balancing DA and ACh signaling. Thus, the behavioral deficits seen in models of PD[94] and in PD patients[95] could stem in part from a suppression of striatal NO signaling. The observation that NO signaling and its regulation of synaptic plasticity was effectively alleviated by the combination of a D1R agonist and mAChR antagonist has clear-cut implications for PD treatment regimens.

Limitations of the study

There are several limitations of our study that need to be considered. At present, there is no reliable method for directly monitoring NO release by LTSIs and the resulting changes in intracellular cGMP in SPNs. Being able to monitor these parameters would have provided important information about the spatial distribution of NO/cGMP signaling in SPN dendrites, which appears to be non-uniform. Another limitation is that the normal role of SPN NO/cGMP signaling in controlling striatum-regulated behavior, like reinforcement learning and reversal learning, was not assessed. Although feasible and important, these studies were beyond our scope.

STAR★METHODS

RESOURCE AVAILABILITY

Lead contact—Further information and requests for resources and reagents may be directed to and will be fulfilled by the Lead Contact, Dr. D. James Surmeier (j-surmeier@northwestern.edu).

Materials availability—Request for *Cacna1d*$^{G407R/+}$ mice should be addressed to Dr. Anis Contractor (a-contractor@northwestern.edu); request for DEAC450-cGMP should be addressed to Dr. Graham Ellis-Davies (graham.ellis-davies@mssm.edu); request for

Author Manuscript Author Manuscript Author Manuscript Author Manuscript

$Ca_V1.3^{fL/fL}$ mice and all other materials should be addressed to Dr. D. James Surmeier (j-surmeier@northwestern.edu).

Data and code availability

- Detailed dataset reported in this paper are available from the lead contact upon request.
- The NEURON + Python model of a reconstructed SPN is available at: https://github.com/vernonclarke/SPNcell/tree/v1.0; Zenodo: https://doi.org/10.5281/zenodo.12213216
- Any additional information required to reanalyze the data reported in this paper is available from the lead contact upon request.

EXPERIMENTAL MODEL AND STUDY PARTICIPANT DETAILS

Animals subjects—All procedures were approved by the Northwestern Institutional Animal Care and Use committee. Mice (6–14 weeks of age) used in *ex vivo* experiments (except Figures 2E, 3H–3J, and 7E–7G) were C57Bl/6 hemizygous mice expressing tdTomato or eGFP under control of Drd1a or Drd2 receptor regulator elements (RRID: MMRRC_030512-UNC and RRID: MMRRC_000230-UNC, backcrossed to C57BL/6 background). In some experiments, these mice were crossed with Thy1-ChR2-YFP mice (B6.Cg-Tg(Thy1-COP4/EYFP) 18Gfng/J, RRID:IMSR_JAX:007612), $Cacna1d^{G407R/+}$ mice (generated in-house), or Tg(Grp-cre)KH288Gsat (MMRRC, RRID: MMRRC_031183_UCD). In Figure 2E, ChAT-Cre × Ai14 mice (cross of RRID: IMSR_JAX:006410 and RRID: IMSR_JAX:007908) were used to identify ChIs. In Figures 3H–3J, $Ca_V1.3^{fL/fL}$ mice generated in-house were used. In Figures 7E–7G, NPY-EGFP mice (RRID: IMSR_JAX:006417) were used to identify LTSIs. Both male and female mice were used for experiments.

METHOD DETAILS

Brain slice preparation—The mice were anesthetized with intraperitoneal injection of a mixture of ketamine (100 mg kg^{-1}) and xylazine (7 mg kg^{-1}) and perfused transcardially with ice-cold cutting solution containing (in mM): 110 choline chloride, 25 $NaHCO_3$, 1.25 NaH_2PO_4, 2.5 KCl, 0.5 $CaCl_2$, 7 $MgCl_2$, 11.6 sodium ascorbate, 3.1 sodium pyruvate and 5 glucose (305 mOsm L^{-1}). Parasagittal brain slices (280-μm thick) were cut by a Leica vibratome (VT1200S, Leica Biosystems, Wetzlar, Germany) and then incubated for 40 min at 34°C in artificial cerebrospinal fluid (ACSF) containing (in mM): 124 NaCl, 3 KCl, 1 NaH_2PO_4, 2.0 $CaCl_2$, 1.0 $MgCl_2$, 26 $NaHCO_3$ and 13.89 glucose, after which they were stored at room temperature for at least 30 min before recording. All external solutions were oxygenated with carbogen (95%CO_2/5%O_2) the entire time.

Electrophysiology—Individual slices were transferred to a recording chamber and continuously superfused with ACSF (2–3 mL/min, 31°C–32°C). D1-Tdtomato- or D2-eGFP-expressing SPNs in the striatum were first identified with an Olympus BX-51-based two-photon laser scanning microscope (Ultima, Bruker Nano fluorescence). Whole-cell patch clamp was then performed in identified SPNs, aided by visualization with a 60X/

Author Manuscript Author Manuscript Author Manuscript Author Manuscript

0.9NA water-dipping objective lens and a ½" CCD video camera (Hitachi) imaged through a Dodt contrast tube and a 2× magnification changer (Bruker). All EPSC recordings were acquired in the presence of picrotoxin (50 μM) in the bath to suppress $GABA_A$-mediated currents. For cGMP-mediated LTD recordings, patch pipettes (3–4 MΩ resistance) were loaded with an internal solution containing (in mM): 120 $CsCH_3SO_3$, 5 NaCl, 0.25 EGTA, 10 HEPES, 4 Mg-ATP, 0.3 Na-GTP, 10 TEA, 5 QX-314 (pH 7.25, osmolarity 280–290 mOsm L^{-1}). SPNs were held at −70 mV (except in Figures 3F and 3G). For eCB-LTD experiments, patch pipettes (3–4 MΩ resistance) were loaded with an internal solution containing (in mM): 126 $CsCH_3SO_3$, 8 NaCl, 10 HEPES, 2.9 QX-314, 8 Na-phosphocreatine, 0.3 Na-GTP, 4 Mg-ATP, 0.1 $CaCl_2$, 1 EGTA (pH 7.2–7.3, osmolarity 285–290 mOsm L^{-1}).[19] SPNs were held at −50 mV (Figure S6A) or −60 mV (Figures 4I, 4J, and S6B) throughout the recordings. For cell-attached recordings of ChIs and LTSIs, interneurons were identified by their fluorescence, distinctive somatodendritic morphology and presence of spontaneous firing. Patch pipettes (~4 MΩ resistance) were loaded with a solution containing (mM): 115 K-gluconate, 20 KCl, 1.5 $MgCl_2$,5 HEPES, 0.2 EGTA, 2 Mg-ATP, 0.5 Na-GTP, 10 Na-phosphocreatine (pH 7.25, osmolarity 280–290 mOsm L^{-1}). All the recordings were made using a MultiClamp 700B amplifier (Axon Instrument, USA), and signals were filtered at 2 kHz and digitized at 10 kHz. Voltage clamp protocols and data acquisition were performed by *Prairie View* 5.3 (Bruker). Data were included if the series resistance (<20 MU) changed less than 20% and the holding current changed less than 100 pA over the course of the experiment. EPSCs were evoked every 20 s by single 0.3-ms pulses of whole-field LED illumination or by paired electrical pulses (50 ms inter-stimulus interval) from a concentric bipolar electrode placed in Layer 5 of the overlying cortex. LED intensity and stimulus current were adjusted to yield EPSC amplitudes between 100 and 400 pA. EPSC amplitudes were normalized to the average EPSC of the baseline recording. The three normalized EPSCs from every minute were averaged to provide each data point in the LTD time course graphs.

Whole-cell cGMP uncaging—The internal solution was supplemented with 75 μM DEAC450-cGMP. To avoid unintended photolysis of DEAC450-cGMP, internal solution preparation and patching were performed under red-light (630 nm) or orange-light (550 nm) illumination within a dark room. At the time of uncaging, patched cells have been filled with DEAC450-cGMP for at least 15 min. Whole-cell intracellular uncaging of DEAC450-cGMP was achieved with 200-ms pulses of 470/30 nm LED light (pE-100, CoolLED) at an intensity of 11.3 mW/mm^2 measured at the objective lens (with a field of view of 366 μm diameter). For LTD induction, a total of five LED uncaging light pulses were applied at 1-min interval.

Dual-color uncaging of glutamate and cGMP—The internal solution was supplemented with 75 μM DEAC450-cGMP and 50 μM Alexa Fluor 594 (Thermo Fisher Scientific). To avoid unintended photolysis of caged cGMP, the recorded SPN was visualized using a 1040-nm excitation laser (Chameleon-Ultra1, Coherent) from a two-photon laser scanning microscope (Ultima, Bruker) and a 60X/0.9 NA objective (Olympus). MNI-glutamate (5mM, Tocris), dissolved in HEPES-buffered ACSF, was superfused over the recorded region through a syringe pump (SP100i, World Precision Instruments), and a

Author Manuscript Author Manuscript Author Manuscript Author Manuscript

three-dimensionally localized volume of glutamate was photolyzed by 1ms exposures from a separate two-photon-excitation laser (Verdi/Mira, Coherent) tuned to 720 nm as previously reported.[7] Baseline 2pEPSC was recorded and averaged from four coplanar dendritic spines (~50–60 μm from soma), each averaged 4 times (10 s inter-sweep interval). Localized dendritic uncaging of DEAC450-cGMP was initiated with 100-ms exposure of collimated 473 nm laser beam (Aurora, Prairie Technologies) at a light intensity of <28 mW/mm^2. A series of five 473 nm laser spots (each spot being ~7 μm in diameter, 100 ms in duration) was applied to cover a dendritic segment of ~35 μm. Similar to the whole-cell cGMP uncaging, five uncaging epochs were applied at 1-min interval to induce LTD. At the end of each experiment, a maximum projection image (199.2 μm × 199.2 μm) of the SPN was acquired with 0.389 μm × 0.389 μm pixels, 1 μm z-steps, and 4 μs/pixel dwell time.

Two-photon laser scanning Ca^{2+} imaging—The pipette solution (EGTA omitted) was supplemented with 100 μM calcium-sensitive dye Fluo-4 or Fura-2 (Thermo Fisher Scientific) and 50 μM calcium-insensitive dye Alexa Fluor 568 (Thermo Fisher Scientific). After whole-cell recording configuration was established, cells were allowed to equilibrate with dyes for at least 15 min before imaging. The recorded SPN was visualized using 810 nm (for Fluo-4 imaging) or 780 nm (for Fura-2 imaging) excitation (Chameleon-Ultra1, Coherent). Dendritic structure was visualized by the red signal of Alexa Fluor 568 detected by a Hamamatsu R3982 side-on photomultiplier tube (PMT, 580–620 nm). Calcium transients, as signals in the green channel, were detected by a Hamamatsu H7422P-40 GaAsP PMT (490–560 nm, Hamamatsu Photonics, Japan). Signals from both channels were background subtracted before analysis. Line scan signals were acquired with 128 pixels per line resolution and 10 μs/pixel dwell time along a dendritic segment. Ca^{2+} signals were quantified as the area of increase in green fluorescence from baseline normalized by the average red fluorescence (ΔG/R) or the average baseline green fluorescence ($\Delta F/F_0$).[22]

Stereotaxic viral injection—Mice (8–12 weeks old) were anesthetized using an isoflurane precision vaporizer (at 5% isoflurane during induction and 2% isoflurane during maintenance phase) and positioned in a stereotaxic frame (Model 940, David Kopf Instruments). Mice were administered with meloxicam (METACAM, 0.1 mg/kg, s.c., Covetrus) before surgery. After the skin and fascia were retracted to reveal the skull, a small hole was drilled, and an injection needle was slowly inserted. For studying synaptic responses at corticostriatal synapses, 0.15 μL AAV5-hSyn-hChR2(H134R)-EYFP (Addgene #26973) was injected into the M1 motor cortex at the following coordinates (mm relative to bregma): ML 1.60, AP 1.15, DV 1.55. For studying synaptic responses at PFN-SPN synapses, 0.1 μL Cre-off virus AAV9-floxed-cre off-hEF1a-ChR2-EYFP-WRE-pA (Virovek, USA) was injected into the PFN of KH288 Grp-Cre mice at the following coordinates (mm relative to bregma): ML 0.64, AP −2.23, DV 3.20. For RiboTag experiments, AAV9-EF1a-DIO-Rpl22L1-myc-FLag-2A-tdTomato (Virovek, USA) was injected into the striatum of A2a-Cre mice at the following coordinates (mm relative to bregma): ML 2.3, AP 1, DV 3.2. For $Ca_V1.3$ deletion, AAV9-CMV-Cre-2A-Tdtomato was injected into the dorsolateral striatum of $Ca_V1.3^{fL/fL}$ mice at the following coordinates (mm relative to bregma): ML 2.4, AP 0.8, DV 3.2.The injection needle was left in place for 5 min to allow tissue absorption of the virus, and then withdrawn. The mice were then sutured up and left on a heating pad until

Author Manuscript Author Manuscript Author Manuscript Author Manuscript

recovery from anesthesia. Experiments were performed three weeks (for Cre-independent infection) or four to five weeks (for Cre-dependent infection) after viral injection.

RiboTag profiling—The AAV for expressing RiboTag under a Cre-dependent promoter (AAV9-EF1a-DIO-Rpl22L1-Myc-DDK-2A-tdTomato-WPRE, titers 2.24 + 10^{13} viral genome/mL) was stereotaxically injected into the striatum of A2a-Cre or A2a-Cre × $Ca_V1.3^{fL/fL}$ mice as described above. Four weeks after injection, mice were sacrificed and the striatal tissue expressing RiboTag was dissected and frozen at −80°C. RiboTag immunoprecipitation was carried out as previously described.[49] Briefly, tissue was homogenized in cold homogenization buffer (50 mM Tris at pH 7.4, 100 mM KCl, 10 mM $MgCl_2$, 1 mM dithiothreitol, 100 μg/mL cycloheximide, protease inhibitors, and recombinant RNase inhibitors, 1% NP-40). Homogenates were centrifuged at 10,000× g for 10 min, the supernatant was collected and precleared with Protein G magnetic beads (Thermo Fisher Scientific) for 1 h at 4°C, under constant rotation. Immunoprecipitations were carried out with anti-Flag magnetic beads (Sigma-Aldrich) at 4°C overnight with constant rotation, followed by four washes in high salt buffer (50 mM Tris at pH 7.4, 350 mM KCl, 10 mM $MgCl_2$, 1% NP-40, 1 mM dithiothreitol, 100 μg/mL cycloheximide). RNA was extracted using RNA-easy Micro RNA extraction kit (QIAGEN) according to manufacturer's instructions.

Quantitative real-time PCR—RNA was extracted from the dissected striatum tissue using RNeasy Micro kit (QIAGEN). Complementary DNA (cDNA) was synthetized by using the Superscript IV VILO Master Mix (Thermo Fisher Scientific) and pre-amplified for 9 cycles using TaqMan PreAmp Master Mix and pool of TaqMan Gene Expression Assays (Thermo Fisher Scientific). The resulting product was diluted and then used for PCR with the corresponding TaqMan Gene Expression Assay and TaqMan Fast Advanced Master Mix (Thermo Fisher Scientific). Data were normalized to hypoxanthine phosphoribosyltransferase 1 (HPRT) by the comparative the $2^{-\Delta\Delta Ct}$ method.[96] The following TaqMan probes were used for PCR amplification of genes: HPRT, Mm03024075_m1; $Ca_V1.2$, Mm01188822_m1; $Ca_V3.1$, Mm00486549_m1; and $Ca_V1.3$, custom made (upper CCTGATTATTTTTACAGTGGAG, lower TCCATTCCTAACGTAAGCAT, probe ATAGCGTATGGACTGTTGCTG). Experimental Ct values were normalized to HPRT values using the formula: ΔCt = Ct ($Ca_V1.2$ or $Ca_V1.3$ or $Ca_V3.1$) – Ct (HPRT). Each ΔCt was then compared to the averaged ΔCt of the control group to obtain the ΔΔCt values: ΔΔCt = ΔCt-averaged ΔCt of control. The final expression levels were shown as $2^{-\Delta\Delta Ct}$.

Immunostaining and confocal microscopy—Anesthetized mice were perfused transcardially with saline briefly (~1 min) and then with ice-cold 4% paraformaldehyde (w/v) in 1x phosphate buffered saline (4% PFA-PBS). Brains were dissected out and post-fixed in 4% PFA-PBS overnight at 4°C. Immunostaining was performed using methods described previously.[97] Briefly, sagittal or coronal slices (100 mm-thick) were cut using a Leica vibratome, permeabilized and blocked at 4°C in PBS including 5% normal goat serum and 0.2% Triton X-100 (NGS/PBST), incubated with rabbit monoclonal anti-PDE1B antibody (ab182565, Abcam) diluted 1:200 in NGS-PBST overnight at 4°C. After four washes in NGS/PBST, the slices were incubated with 1:1000 goat anti-rabbit Alexa Fluor

Author Manuscript Author Manuscript Author Manuscript Author Manuscript

488 or 555 (A-11008 and A-21428, Invitrogen) for 2 h at room temperature. Slices were washed with NGS-PBST four times and PBS once, mounted with VECTASHIELD Mounting Medium (Vector Laboratories), and viewed under an automated laser scanning confocal microscope (FV10i; Olympus). Images were adjusted for brightness, contrast, and pseudo-coloring in ImageJ (US National Institutes of Health).

Western blotting—Striatum tissues from *Cacna1d*$^{G407R/+}$ mice and wildtype siblings were collected and homogenized in N-Per Neuronal protein extraction buffer (Thermo Fisher Scientific) supplemented with Protease inhibitors (Halt Protease and Phosphatase Inhibitor Cocktail, Thermo Fisher Scientific). Samples were prepared in NuPAGE LDS Sample Buffer (Invitrogen) and separated by SDS-PAGE. Primary antibodies to PDE1B (1:1000, ab182565, Abcam) and GAPDH (1:1000, #2118, Cell Signaling) were used for Western blotting. Target protein bands were visualized with horseradish peroxidase-conjugated secondary antibodies (#7074, Cell Signaling) and enhanced chemiluminescent reagent SuperSignal West Dura (Thermo Fisher Scientific). Intensities of the target protein bands were detected with Odyssey Fc (Li-Cor) and quantified in Image Studio (Li-Cor).

Development of $Ca_V1.3^{fL/fL}$ mice—The final targeting vector for conditional deletion of *Cacna1d* was purchased from EuMMCR (https://www.eummcr.org/search?q=PG00090_Y_4_H05&b=Search). The embryonic stem (ES) cell targeting and injection were performed by the Northwestern University Transgenic and Targeted Mutagenesis Laboratory. The targeting vector DNA was electroporated into PRX-B6N ES cells. Colonies that survived G418 selection were chosen and genotyped. After the correct targeting was confirmed, ES cells were injected into albino B6 (B6(Cg)-*Tyr*$^{c-2J}$/J–000058 from The Jackson Laboratory) blastocysts and resulted in the generation of highly chimeric males (80–100% black in color). The chimera were then bred with albino B6 mice. The mutant offsprings were then mated with FLP recombinase transgenic mice to convert the unconditional allele into a conditional allele. The heterozygous conditional mice were then mated to generate homozygous ($Ca_V1.3^{fL/fL}$) mice.

Development of *Cacna1d*$^{G407R/+}$ mice—The CRISPR/Cas9 gene editing system was used to generate the G407R amino acid substitution in the mouse *Cacna1d* gene.[98] The glycine at position 407 (G407) is coded by two separate exons, with dinucleotide GG from exon 8 and a single nucleotide A from exon 9 making up the codon. A GG to AG mutation was introduced in exon 8 that results in a glycine to arginine substitution at this site (G407R) (Figure S5A). Single guide RNAs (gRNA) (Figure S5B), Cas9 mRNA and a single strand oligonucleotide donor (ss donor) with a single base mutation (G407 to R407) were microinjected into mouse zygotes. Two female founders with the positively identified G407R mutation were bred with wildtype C57/bl6J mice, and each of these founders have produced viable heterozygous and homozygous G407R mutant mice (see Figure S5C for a representative DNA sequencing chromatogram).

Modeling—The NEURON (Neuron 8.2; RRID:SCR_005393)[99] + Python (Python Programming Language RRID:SCR_008394) model of a morphologically reconstructed SPN[67] was built upon a previously established model.[65,100,101] The model was

Author Manuscript Author Manuscript Author Manuscript Author Manuscript

essentially unchanged from the previously version (for details see ref.[67]; https://github.com/vernonclarke/SPNcell/tree/v1.0; Zenodo: https://doi.org/10.5281/zenodo.12213216). The number of compartments was increased slightly (~820).

QUANTIFICATION AND STATISTICAL ANALYSIS

Electrophysiology and imaging data were acquired using PCI-NI6052E analog-to-digital converter card (National Instruments) and *Praire View* 5.3 (Bruker). Offline analysis of electrophysiology data was performed using Clampfit 10.5 (Molecular Devices) and Origin 8 or 2020 (OriginLab). Time course data were presented as mean ± SEM, and quantification data as non-parametric box-whisker plots. Offline analysis of calcium imaging data was performed by custom-written Python script (available upon request), and statistical analysis performed by Prism 6 or 9 (GraphPad). The stated n indicates the number of cells (in electrophysiology experiments) or the number of dendrites (in calcium imaging experiments). Nonparametric tests (Mann-Whitney U test or Wilcoxon signed rank test for non-paired or paired design experiments, respectively) were used due to small sample sizes, unless otherwise stated. The statistical significance was considered as $p < 0.05$ (*), $p < 0.01$ (**) and $p < 0.001$ (***).

Supplementary Material

Refer to Web version on PubMed Central for supplementary material.

ACKNOWLEDGMENTS

We thank the members of the Surmeier lab and Dr. Richard B. Silverman for their support and comments on the manuscript. We thank Dr. Paul T. Schumacker and the Northwestern Transgenic & Targeted Mutagenesis Core Facility for their help in the generation of the $Ca_V1.3$ floxed mice. We also thank Lundbeck for generously providing the PDE1B inhibitor AF64196. This work is supported by the JPB Foundation (to D.J.S.), NIH NS34696 (to D.J.S.), the William N. and Bernice E. Bumpus Foundation (to D.J.S and S.Z.), DOD W81XWH-18-1-0777 (to A.C. and D.J.S.), NIH/National Institute of Mental Health R01MH099114 (to A.C. and D.J.S.), the Simons Foundation (to A.C.), NIH/National Institute of General Medical Sciences RO1 GM053395, and NIH/National Institute of Neurological Disorders and Stroke R35 NS111600 (to G.C.R.E.-D.).

REFERENCES

1. Balleine BW, Delgado MR, and Hikosaka O (2007). The role of the dorsal striatum in reward and decision-making. J. Neurosci. 27, 8161–8165. 10.1523/JNEUROSCI.1554-07.2007. [PubMed: 17670959]
2. Reynolds JN, and Wickens JR (2002). Dopamine-dependent plasticity of corticostriatal synapses. Neural Network. 15, 507–521. 10.1016/s0893-6080(02)00045-x.
3. Graybiel AM, and Grafton ST (2015). The striatum: where skills and habits meet. Cold Spring Harbor Perspect. Biol. 7, a021691. 10.1101/cshperspect.a021691.
4. Cox J, and Witten IB (2019). Striatal circuits for reward learning and decision-making. Nat. Rev. Neurosci. 20, 482–494. 10.1038/s41583-019-0189-2. [PubMed: 31171839]
5. Pisani A, Centonze D, Bernardi G, and Calabresi P (2005). Striatal synaptic plasticity: implications for motor learning and Parkinson's disease. Mov. Disord. 20, 395–402. 10.1002/mds.20394. [PubMed: 15719415]
6. Lovinger DM (2010). Neurotransmitter roles in synaptic modulation, plasticity and learning in the dorsal striatum. Neuropharmacology 58, 951–961. 10.1016/j.neuropharm.2010.01.008. [PubMed: 20096294]

Author Manuscript Author Manuscript Author Manuscript Author Manuscript

7. Plotkin JL, Day M, and Surmeier DJ (2011). Synaptically driven state transitions in distal dendrites of striatal spiny neurons. Nat. Neurosci. 14, 881–888. 10.1038/nn.2848. [PubMed: 21666674]
8. Perrin E, and Venance L (2019). Bridging the gap between striatal plasticity and learning. Curr. Opin. Neurobiol. 54, 104–112. 10.1016/j.conb.2018.09.007. [PubMed: 30321866]
9. Surmeier DJ, Plotkin J, and Shen W (2009). Dopamine and synaptic plasticity in dorsal striatal circuits controlling action selection. Curr. Opin. Neurobiol. 19, 621–628. 10.1016/j.conb.2009.10.003. [PubMed: 19896832]
10. Zhai S, Tanimura A, Graves SM, Shen W, and Surmeier DJ (2018). Striatal synapses, circuits, and Parkinson's disease. Curr. Opin. Neurobiol. 48, 9–16. 10.1016/j.conb.2017.08.004. [PubMed: 28843800]
11. Calabresi P, Maj R, Pisani A, Mercuri NB, and Bernardi G (1992). Long-term synaptic depression in the striatum: physiological and pharmacological characterization. J. Neurosci. 12, 4224–4233. [PubMed: 1359031]
12. Choi S, and Lovinger DM (1997). Decreased probability of neurotransmitter release underlies striatal long-term depression and postnatal development of corticostriatal synapses. Proc. Natl. Acad. Sci. USA 94, 2665–2670. 10.1073/pnas.94.6.2665. [PubMed: 9122253]
13. Gerdeman G, and Lovinger DM (2001). CB1 cannabinoid receptor inhibits synaptic release of glutamate in rat dorsolateral striatum. J. Neurophysiol. 85, 468–471. 10.1152/jn.2001.85.1.468. [PubMed: 11152748]
14. Kreitzer AC, and Malenka RC (2005). Dopamine modulation of state-dependent endocannabinoid release and long-term depression in the striatum. J. Neurosci. 25, 10537–10545. 10.1523/JNEUROSCI.2959-05.2005. [PubMed: 16280591]
15. Kreitzer AC, and Malenka RC (2007). Endocannabinoid-mediated rescue of striatal LTD and motor deficits in Parkinson's disease models. Nature 445, 643–647. 10.1038/nature05506. [PubMed: 17287809]
16. Lerner TN, and Kreitzer AC (2012). RGS4 is required for dopaminergic control of striatal LTD and susceptibility to parkinsonian motor deficits. Neuron 73, 347–359. 10.1016/j.neuron.2011.11.015. [PubMed: 22284188]
17. Shen W, Flajolet M, Greengard P, and Surmeier DJ (2008). Dichotomous dopaminergic control of striatal synaptic plasticity. Science 321, 848–851. 10.1126/science.1160575. [PubMed: 18687967]
18. Rafalovich IV, Melendez AE, Plotkin JL, Tanimura A, Zhai S, and Surmeier DJ (2015). Interneuronal Nitric Oxide Signaling Mediates Post-synaptic Long-Term Depression of Striatal Glutamatergic Synapses. Cell Rep. 13, 1336–1342. 10.1016/j.celrep.2015.10.015. [PubMed: 26549446]
19. Wu YW, Kim JI, Tawfik VL, Lalchandani RR, Scherrer G, and Ding JB (2015). Input- and cell-type-specific endocannabinoid-dependent LTD in the striatum. Cell Rep. 10, 75–87. 10.1016/j.celrep.2014.12.005. [PubMed: 25543142]
20. Wang Z, Kai L, Day M, Ronesi J, Yin HH, Ding J, Tkatch T, Lovinger DM, and Surmeier DJ (2006). Dopaminergic control of corticostriatal long-term synaptic depression in medium spiny neurons is mediated by cholinergic interneurons. Neuron 50, 443–452. 10.1016/j.neuron.2006.04.010. [PubMed: 16675398]
21. Adermark L, and Lovinger DM (2007). Combined activation of L-type Ca2+ channels and synaptic transmission is sufficient to induce striatal long-term depression. J. Neurosci. 27, 6781–6787. 10.1523/JNEUROSCI.0280-07.2007. [PubMed: 17581965]
22. Plotkin JL, Shen W, Rafalovich I, Sebel LE, Day M, Chan CS, and Surmeier DJ (2013). Regulation of dendritic calcium release in striatal spiny projection neurons. J. Neurophysiol. 110, 2325–2336. 10.1152/jn.00422.2013. [PubMed: 23966676]
23. Calabresi P, Gubellini P, Centonze D, Sancesario G, Morello M, Giorgi M, Pisani A, and Bernardi G (1999). A critical role of the nitric oxide/cGMP pathway in corticostriatal long-term depression. J. Neurosci. 19, 2489–2499. [PubMed: 10087063]
24. Lakics V, Karran EH, and Boess FG (2010). Quantitative comparison of phosphodiesterase mRNA distribution in human brain and peripheral tissues. Neuropharmacology 59, 367–374. 10.1016/j.neuropharm.2010.05.004. [PubMed: 20493887]

Author Manuscript Author Manuscript Author Manuscript Author Manuscript

25. Polli JW, and Kincaid RL (1992). Molecular cloning of DNA encoding a calmodulin-dependent phosphodiesterase enriched in striatum. Proc. Natl. Acad. Sci. USA 89, 11079–11083. 10.1073/pnas.89.22.11079. [PubMed: 1332068]
26. Bender AT, Ostenson CL, Wang EH, and Beavo JA (2005). Selective up-regulation of PDE1B2 upon monocyte-to-macrophage differentiation. Proc. Natl. Acad. Sci. USA 102, 497–502. 10.1073/pnas.0408535102. [PubMed: 15625104]
27. Soderling SH, Bayuga SJ, and Beavo JA (1999). Isolation and characterization of a dual-substrate phosphodiesterase gene family: PDE10A. Proc. Natl. Acad. Sci. USA 96, 7071–7076. 10.1073/pnas.96.12.7071. [PubMed: 10359840]
28. Goraya TA, and Cooper DM (2005). Ca2+-calmodulin-dependent phosphodiesterase (PDE1): current perspectives. Cell. Signal. 17, 789–797. 10.1016/j.cellsig.2004.12.017. [PubMed: 15763421]
29. Sharma RK, Das SB, Lakshmikuttyamma A, Selvakumar P, and Shrivastav A (2006). Regulation of calmodulin-stimulated cyclic nucleotide phosphodiesterase (PDE1): review. Int. J. Mol. Med. 18, 95–105. [PubMed: 16786160]
30. Calabresi P, Pisani A, Mercuri NB, and Bernardi G (1992). Long-term Potentiation in the Striatum is Unmasked by Removing the Voltage-dependent Magnesium Block of NMDA Receptor Channels. Eur. J. Neurosci. 4, 929–935. 10.1111/j.1460-9568.1992.tb00119.x. [PubMed: 12106428]
31. Carter AG, and Sabatini BL (2004). State-dependent calcium signaling in dendritic spines of striatal medium spiny neurons. Neuron 44, 483–493. 10.1016/j.neuron.2004.10.013. [PubMed: 15504328]
32. Hufgard JR, Williams MT, and Vorhees CV (2017). Phosphodiesterase-1b deletion confers depression-like behavioral resistance separate from stress-related effects in mice. Gene Brain Behav. 16, 756–767. 10.1111/gbb.12391.
33. Hufgard JR, Williams MT, Skelton MR, Grubisha O, Ferreira FM, Sanger H, Wright ME, Reed-Kessler TM, Rasmussen K, Duman RS, and Vorhees CV (2017). Phosphodiesterase-1b (Pde1b) knockout mice are resistant to forced swim and tail suspension induced immobility and show upregulation of Pde10a. Psychopharmacology (Berl) 234, 1803–1813. 10.1007/s00213-017-4587-8. [PubMed: 28337525]
34. Heiman M, Schaefer A, Gong S, Peterson JD, Day M, Ramsey KE, Suarez-Farinas M, Schwarz C, Stephan DA, Surmeier DJ, et al. (2008). A translational profiling approach for the molecular characterization of CNS cell types. Cell 135, 738–748. 10.1016/j.cell.2008.10.028. [PubMed: 19013281]
35. Yan C, Bentley JK, Sonnenburg WK, and Beavo JA (1994). Differential expression of the 61 kDa and 63 kDa calmodulin-dependent phosphodiesterases in the mouse brain. J. Neurosci. 14, 973–984. [PubMed: 8120637]
36. Kakkar R, Raju RV, and Sharma RK (1999). Calmodulin-dependent cyclic nucleotide phosphodiesterase (PDE1). Cell. Mol. Life Sci. 55, 1164–1186. 10.1007/s000180050364. [PubMed: 10442095]
37. Bender AT, and Beavo JA (2006). Cyclic nucleotide phosphodiesterases: molecular regulation to clinical use. Pharmacol. Rev. 58, 488–520. 10.1124/pr.58.3.5. [PubMed: 16968949]
38. Ariano MA (1983). Distribution of components of the guanosine 3',5'-phosphate system in rat caudate-putamen. Neuroscience 10, 707–723. 10.1016/0306-4522(83)90212-9. [PubMed: 6139769]
39. Eliasson MJ, Blackshaw S, Schell MJ, and Snyder SH (1997). Neuronal nitric oxide synthase alternatively spliced forms: prominent functional localizations in the brain. Proc. Natl. Acad. Sci. USA 94, 3396–3401. 10.1073/pnas.94.7.3396. [PubMed: 9096405]
40. Matsuoka I, Giuili G, Poyard M, Stengel D, Parma J, Guellaen G, and Hanoune J (1992). Localization of adenylyl and guanylyl cyclase in rat brain by in situ hybridization: comparison with calmodulin mRNA distribution. J. Neurosci. 12, 3350–3360. [PubMed: 1356144]
41. Ding JD, Burette A, Nedvetsky PI, Schmidt HH, and Weinberg RJ (2004). Distribution of soluble guanylyl cyclase in the rat brain. J. Comp. Neurol. 472, 437–448. 10.1002/cne.20054. [PubMed: 15065118]

Author Manuscript Author Manuscript Author Manuscript Author Manuscript

42. Gong S, Zheng C, Doughty ML, Losos K, Didkovsky N, Schambra UB, Nowak NJ, Joyner A, Leblanc G, Hatten ME, and Heintz N (2003). A gene expression atlas of the central nervous system based on bacterial artificial chromosomes. Nature 425, 917–925. 10.1038/nature02033. [PubMed: 14586460]
43. Picconi B, Bagetta V, Ghiglieri V, Paille V, Di Filippo M, Pendolino V, Tozzi A, Giampa C, Fusco FR, Sgobio C, and Calabresi P (2011). Inhibition of phosphodiesterases rescues striatal long-term depression and reduces levodopa-induced dyskinesia. Brain 134, 375–387. 10.1093/brain/awq342. [PubMed: 21183486]
44. Khammy MM, Dalsgaard T, Larsen PH, Christoffersen CT, Clausen D, Rasmussen LK, Folkersen L, Grunnet M, Kehler J, Aalkjaer C, and Nielsen J (2017). PDE1A inhibition elicits cGMP-dependent relaxation of rat mesenteric arteries. Br. J. Pharmacol. 174, 4186–4198. 10.1111/bph.14034. [PubMed: 28910498]
45. Shupliakov O, Low P, Grabs D, Gad H, Chen H, David C, Takei K, De Camilli P, and Brodin L (1997). Synaptic vesicle endocytosis impaired by disruption of dynamin-SH3 domain interactions. Science 276, 259–263. 10.1126/science.276.5310.259. [PubMed: 9092476]
46. Adermark L, and Lovinger DM (2007). Retrograde endocannabinoid signaling at striatal synapses requires a regulated postsynaptic release step. Proc. Natl. Acad. Sci. USA 104, 20564–20569. 10.1073/pnas.0706873104. [PubMed: 18077376]
47. Song RS, Tolentino R, Sobie EA, and Neves-Zaph SR (2016). Cross-regulation of Phosphodiesterase 1 and Phosphodiesterase 2 Activities Controls Dopamine-mediated Striatal alpha-Amino-3-hydroxy-5-methyl-4-isoxazolepropionic Acid (AMPA) Receptor Trafficking. J. Biol. Chem. 291, 23257–23267. 10.1074/jbc.M116.749747. [PubMed: 27605670]
48. Boess FG, Hendrix M, van der Staay FJ, Erb C, Schreiber R, van Staveren W, de Vente J, Prickaerts J, Blokland A, and Koenig G (2004). Inhibition of phosphodiesterase 2 increases neuronal cGMP, synaptic plasticity and memory performance. Neuropharmacology 47, 1081–1092. 10.1016/j.neuropharm.2004.07.040. [PubMed: 15555642]
49. Tanimura A, Du Y, Kondapalli J, Wokosin DL, and Surmeier DJ (2019). Cholinergic Interneurons Amplify Thalamostriatal Excitation of Striatal Indirect Pathway Neurons in Parkinson's Disease Models. Neuron 101, 444–458.e6. 10.1016/j.neuron.2018.12.004. [PubMed: 30658860]
50. Centonze D, Pisani A, Bonsi P, Giacomini P, Bernardi G, and Calabresi P (2001). Stimulation of nitric oxide-cGMP pathway excites striatal cholinergic interneurons via protein kinase G activation. J. Neurosci. 21, 1393–1400. [PubMed: 11160411]
51. Elghaba R, Vautrelle N, and Bracci E (2016). Mutual Control of Cholinergic and Low-Threshold Spike Interneurons in the Striatum. Front. Cell. Neurosci. 10, 111. 10.3389/fncel.2016.00111. [PubMed: 27199665]
52. Agarwal HK, Zhai S, Surmeier DJ, and Ellis-Davies GCR (2017). Intracellular Uncaging of cGMP with Blue Light. ACS Chem. Neurosci. 8, 2139–2144. 10.1021/acschemneuro.7b00237. [PubMed: 28762726]
53. Kakiuchi S, and Yamazaki R (1970). Calcium dependent phosphodiesterase activity and its activating factor (PAF) from brain studies on cyclic 3',5'-nucleotide phosphodiesterase (3). Biochem. Biophys. Res. Commun. 41, 1104–1110. 10.1016/0006-291x(70)90199-3. [PubMed: 4320714]
54. Lipscombe D, Helton TD, and Xu W (2004). L-type calcium channels: the low down. J. Neurophysiol. 92, 2633–2641. 10.1152/jn.00486.2004. [PubMed: 15486420]
55. Day M, Wang Z, Ding J, An X, Ingham CA, Shering AF, Wokosin D, Ilijic E, Sun Z, Sampson AR, et al. (2006). Selective elimination of glutamatergic synapses on striatopallidal neurons in Parkinson disease models. Nat. Neurosci. 9, 251–259. 10.1038/nn1632. [PubMed: 16415865]
56. O'Roak BJ, Vives L, Girirajan S, Karakoc E, Krumm N, Coe BP, Levy R, Ko A, Lee C, Smith JD, et al. (2012). Sporadic autism exomes reveal a highly interconnected protein network of de novo mutations. Nature 485, 246–250. 10.1038/nature10989. [PubMed: 22495309]
57. Pinggera A, Lieb A, Benedetti B, Lampert M, Monteleone S, Liedl KR, Tuluc P, and Striessnig J (2015). CACNA1D de novo mutations in autism spectrum disorders activate Cav1.3 L-type calcium channels. Biol. Psychiatr. 77, 816–822. 10.1016/j.biopsych.2014.11.020.

Author Manuscript Author Manuscript Author Manuscript Author Manuscript

58. Calabresi P, Pisani A, Mercuri NB, and Bernardi G (1994). Post-receptor mechanisms underlying striatal long-term depression. J. Neurosci. 14, 4871–4881. [PubMed: 8046457]

59. Ronesi J, Gerdeman GL, and Lovinger DM (2004). Disruption of endocannabinoid release and striatal long-term depression by postsynaptic blockade of endocannabinoid membrane transport. J. Neurosci. 24, 1673–1679. 10.1523/JNEUROSCI.5214-03.2004. [PubMed: 14973237]

60. Yuste R, and Tank DW (1996). Dendritic integration in mammalian neurons, a century after Cajal. Neuron 16, 701–716. 10.1016/s0896-6273(00)80091-4. [PubMed: 8607989]

61. Sjostrom PJ, Rancz EA, Roth A, and Hausser M (2008). Dendritic excitability and synaptic plasticity. Physiol. Rev. 88, 769–840. 10.1152/physrev.00016.2007. [PubMed: 18391179]

62. Branco T, and Hausser M (2010). The single dendritic branch as a fundamental functional unit in the nervous system. Curr. Opin. Neurobiol. 20, 494–502. 10.1016/j.conb.2010.07.009. [PubMed: 20800473]

63. Olson JP, Kwon HB, Takasaki KT, Chiu CQ, Higley MJ, Sabatini BL, and Ellis-Davies GC (2013). Optically selective two-photon uncaging of glutamate at 900 nm. J. Am. Chem. Soc. 135, 5954–5957. 10.1021/ja4019379. [PubMed: 23577752]

64. Amatrudo JM, Olson JP, Agarwal HK, and Ellis-Davies GC (2015). Caged compounds for multichromic optical interrogation of neural systems. Eur. J. Neurosci. 41, 5–16. 10.1111/ejn.12785. [PubMed: 25471355]

65. Du K, Wu YW, Lindroos R, Liu Y, Rozsa B, Katona G, Ding JB, and Kotaleski JH (2017). Cell-type-specific inhibition of the dendritic plateau potential in striatal spiny projection neurons. Proc. Natl. Acad. Sci. USA 114, E7612–E7621. 10.1073/pnas.1704893114. [PubMed: 28827326]

66. Golding NL, Staff NP, and Spruston N (2002). Dendritic spikes as a mechanism for cooperative long-term potentiation. Nature 418, 326–331. 10.1038/nature00854. [PubMed: 12124625]

67. Day M, Belal M, Surmeier WC, Melendez A, Wokosin D, Tkatch T, Clarke VRJ, and Surmeier DJ (2024). GABAergic regulation of striatal spiny projection neurons depends upon their activity state. PLoS Biol. 22, e3002483. 10.1371/journal.pbio.3002483. [PubMed: 38295323]

68. Moldwin T, Kalmenson M, and Segev I (2023). Asymmetric Voltage Attenuation in Dendrites Can Enable Hierarchical Heterosynaptic Plasticity. eNeuro 10, ENEURO.0014–23.2023. 10.1523/ENEURO.0014-23.2023.

69. Shen W, Plotkin JL, Francardo V, Ko WK, Xie Z, Li Q, Fieblinger T, Wess J, Neubig RR, Lindsley CW, et al. (2015). M4 Muscarinic Receptor Signaling Ameliorates Striatal Plasticity Deficits in Models of L-DOPA-Induced Dyskinesia. Neuron 88, 762–773. 10.1016/j.neuron.2015.10.039. [PubMed: 26590347]

70. Picconi B, Centonze D, Hakansson K, Bernardi G, Greengard P, Fisone G, Cenci MA, and Calabresi P (2003). Loss of bidirectional striatal synaptic plasticity in L-DOPA-induced dyskinesia. Nat. Neurosci. 6, 501–506. 10.1038/nn1040. [PubMed: 12665799]

71. Centonze D, Gubellini P, Picconi B, Calabresi P, Giacomini P, and Bernardi G (1999). Unilateral dopamine denervation blocks corticostriatal LTP. J. Neurophysiol. 82, 3575–3579. 10.1152/jn.1999.82.6.3575. [PubMed: 10601483]

72. Centonze D, Bracci E, Pisani A, Gubellini P, Bernardi G, and Calabresi P (2002). Activation of dopamine D1-like receptors excites LTS interneurons of the striatum. Eur. J. Neurosci. 15, 2049–2052. 10.1046/j.1460-9568.2002.02052.x. [PubMed: 12099911]

73. Melendez-Zaidi AE, Lakshminarasimhah H, and Surmeier DJ (2019). Cholinergic modulation of striatal nitric oxide-producing interneurons. Eur. J. Neurosci. 50, 3713–3731. 10.1111/ejn.14528. [PubMed: 31340071]

74. Ding J, Guzman JN, Tkatch T, Chen S, Goldberg JA, Ebert PJ, Levitt P, Wilson CJ, Hamm HE, and Surmeier DJ (2006). RGS4-dependent attenuation of M4 autoreceptor function in striatal cholinergic interneurons following dopamine depletion. Nat. Neurosci. 9, 832–842. 10.1038/nn1700. [PubMed: 16699510]

75. DeBoer P, Heeringa MJ, and Abercrombie ED (1996). Spontaneous release of acetylcholine in striatum is preferentially regulated by inhibitory dopamine D2 receptors. Eur. J. Pharmacol. 317, 257–262. 10.1016/s0014-2999(96)00761-3. [PubMed: 8997608]

76. van den Pol AN, Yao Y, Fu LY, Foo K, Huang H, Coppari R, Lowell BB, and Broberger C (2009). Neuromedin B and gastrin-releasing peptide excite arcuate nucleus neuropeptide Y neurons in a

Author Manuscript Author Manuscript Author Manuscript Author Manuscript

novel transgenic mouse expressing strong Renilla green fluorescent protein in NPY neurons. J. Neurosci. 29, 4622–4639. 10.1523/JNEUROSCI.3249-08.2009. [PubMed: 19357287]

77. Kawaguchi Y (1993). Physiological, morphological, and histochemical characterization of three classes of interneurons in rat neostriatum. J. Neurosci. 13, 4908–4923. 10.1523/JNEUROSCI.13-11-04908.1993. [PubMed: 7693897]
78. Marletta MA (1994). Nitric oxide synthase: aspects concerning structure and catalysis. Cell 78, 927–930. 10.1016/0092-8674(94)90268-2. [PubMed: 7522970]
79. Diering GH, and Huganir RL (2018). The AMPA Receptor Code of Synaptic Plasticity. Neuron 100, 314–329. 10.1016/j.neuron.2018.10.018. [PubMed: 30359599]
80. Ito M (2001). Cerebellar long-term depression: characterization, signal transduction, and functional roles. Physiol. Rev. 81, 1143–1195. 10.1152/physrev.2001.81.3.1143. [PubMed: 11427694]
81. Polito M, Klarenbeek J, Jalink K, Paupardin-Tritsch D, Vincent P, and Castro LR (2013). The NO/cGMP pathway inhibits transient cAMP signals through the activation of PDE2 in striatal neurons. Front. Cell. Neurosci. 7, 211. 10.3389/fncel.2013.00211. [PubMed: 24302895]
82. Fieblinger T, Perez-Alvarez A, Lamothe-Molina PJ, Gee CE, and Oertner TG (2022). Presynaptic cGMP sets synaptic strength in the striatum and is important for motor learning. EMBO Rep. 23, e54361. 10.15252/embr.202154361. [PubMed: 35735260]
83. Kelly MP, Adamowicz W, Bove S, Hartman AJ, Mariga A, Pathak G, Reinhart V, Romegialli A, and Kleiman RJ (2014). Select 3',5'-cyclic nucleotide phosphodiesterases exhibit altered expression in the aged rodent brain. Cell. Signal. 26, 383–397. 10.1016/j.cellsig.2013.10.007. [PubMed: 24184653]
84. Zhang H, Maximov A, Fu Y, Xu F, Tang TS, Tkatch T, Surmeier DJ, and Bezprozvanny I (2005). Association of CaV1.3 L-type calcium channels with Shank. J. Neurosci. 25, 1037–1049. 10.1523/JNEUROSCI.4554-04.2005. [PubMed: 15689539]
85. Day M, Wokosin D, Plotkin JL, Tian X, and Surmeier DJ (2008). Differential excitability and modulation of striatal medium spiny neuron dendrites. J. Neurosci. 28, 11603–11614. 10.1523/JNEUROSCI.1840-08.2008. [PubMed: 18987196]
86. Dauer W, and Przedborski S (2003). Parkinson's disease: mechanisms and models. Neuron 39, 889–909. 10.1016/s0896-6273(03)00568-3. [PubMed: 12971891]
87. Maurice N, Mercer J, Chan CS, Hernandez-Lopez S, Held J, Tkatch T, and Surmeier DJ (2004). D2 dopamine receptor-mediated modulation of voltage-dependent Na+ channels reduces autonomous activity in striatal cholinergic interneurons. J. Neurosci. 24, 10289–10301. 10.1523/JNEUROSCI.2155-04.2004. [PubMed: 15548642]
88. Chuhma N, Mingote S, Moore H, and Rayport S (2014). Dopamine neurons control striatal cholinergic neurons via regionally heterogeneous dopamine and glutamate signaling. Neuron 81, 901–912. 10.1016/j.neuron.2013.12.027. [PubMed: 24559678]
89. Pisani A, Bernardi G, Ding J, and Surmeier DJ (2007). Re-emergence of striatal cholinergic interneurons in movement disorders. Trends Neurosci. 30, 545–553. 10.1016/j.tins.2007.07.008. [PubMed: 17904652]
90. Sanchez-Catasus CA, Bohnen NI, D'Cruz N, and Muller M (2022). Striatal Acetylcholine-Dopamine Imbalance in Parkinson Disease: In Vivo Neuroimaging Study with Dual-Tracer PET and Dopaminergic PET-Informed Correlational Tractography. J. Nucl. Med. 63, 438–445. 10.2967/jnumed.121.261939. [PubMed: 34272323]
91. Sammut S, Dec A, Mitchell D, Linardakis J, Ortiguela M, and West AR (2006). Phasic dopaminergic transmission increases NO efflux in the rat dorsal striatum via a neuronal NOS and a dopamine D(1/5) receptor-dependent mechanism. Neuropsychopharmacology 31, 493–505. 10.1038/sj.npp.1300826. [PubMed: 16012530]
92. Sagi Y, Heiman M, Peterson JD, Musatov S, Scarduzio M, Logan SM, Kaplitt MG, Surmeier DJ, Heintz N, and Greengard P (2014). Nitric oxide regulates synaptic transmission between spiny projection neurons. Proc. Natl. Acad. Sci. USA 111, 17636–17641. 10.1073/pnas.1420162111. [PubMed: 25413364]
93. Sancesario G, Giorgi M, D'Angelo V, Modica A, Martorana A, Morello M, Bengtson CP, and Bernardi G (2004). Down-regulation of nitrergic transmission in the rat striatum after chronic

Author Manuscript Author Manuscript Author Manuscript Author Manuscript

nigrostriatal deafferentation. Eur. J. Neurosci. 20, 989–1000. 10.1111/j.1460-9568.2004.03566.x. [PubMed: 15305867]

94. Clarke HF, Hill GJ, Robbins TW, and Roberts AC (2011). Dopamine, but not serotonin, regulates reversal learning in the marmoset caudate nucleus. J. Neurosci. 31, 4290–4297. 10.1523/JNEUROSCI.5066-10.2011. [PubMed: 21411670]
95. Peterson DA, Elliott C, Song DD, Makeig S, Sejnowski TJ, and Poizner H (2009). Probabilistic reversal learning is impaired in Parkinson's disease. Neuroscience 163, 1092–1101. 10.1016/j.neuroscience.2009.07.033. [PubMed: 19628022]
96. Livak KJ, and Schmittgen TD (2001). Analysis of relative gene expression data using real-time quantitative PCR and the 2(-Delta Delta C(T)) Method. Methods 25, 402–408. 10.1006/meth.2001.1262. [PubMed: 11846609]
97. Zhai S, Ark ED, Parra-Bueno P, and Yasuda R (2013). Long-distance integration of nuclear ERK signaling triggered by activation of a few dendritic spines. Science 342, 1107–1111. 10.1126/science.1245622. [PubMed: 24288335]
98. Wang H, Yang H, Shivalila CS, Dawlaty MM, Cheng AW, Zhang F, and Jaenisch R (2013). One-step generation of mice carrying mutations in multiple genes by CRISPR/Cas-mediated genome engineering. Cell 153, 910–918. 10.1016/j.cell.2013.04.025. [PubMed: 23643243]
99. Hines ML, and Carnevale NT (1997). The NEURON simulation environment. Neural Comput. 9, 1179–1209. 10.1162/neco.1997.9.6.1179. [PubMed: 9248061]
100. Lindroos R, Dorst MC, Du K, Filipovic M, Keller D, Ketzef M, Kozlov AK, Kumar A, Lindahl M, Nair AG, et al. (2018). Basal Ganglia Neuromodulation Over Multiple Temporal and Structural Scales-Simulations of Direct Pathway MSNs Investigate the Fast Onset of Dopaminergic Effects and Predict the Role of Kv4.2. Front. Neural Circ. 12, 3. 10.3389/fncir.2018.00003.
101. Lindroos R, and Hellgren Kotaleski J (2021). Predicting complex spikes in striatal projection neurons of the direct pathway following neuromodulation by acetylcholine and dopamine. Eur. J. Neurosci. 53, 2117–2134. 10.1111/ejn.14891 . [PubMed: 32609903]

Author Manuscript Author Manuscript Author Manuscript Author Manuscript

Highlights

- cGMP-dependent LTD of striatal glutamatergic synapses was controlled by PDE1
- The activity of PDE1 was regulated by Ca^{2+} influx through $Ca_V1.3$ Ca^{2+} channels
- This coupling limited cGMP-dependent LTD to dendritic regions that were inactive
- Reversing neuromodulatory imbalance restored cGMP-LTD in a Parkinson's disease model

Author Manuscript Author Manuscript Author Manuscript Author Manuscript

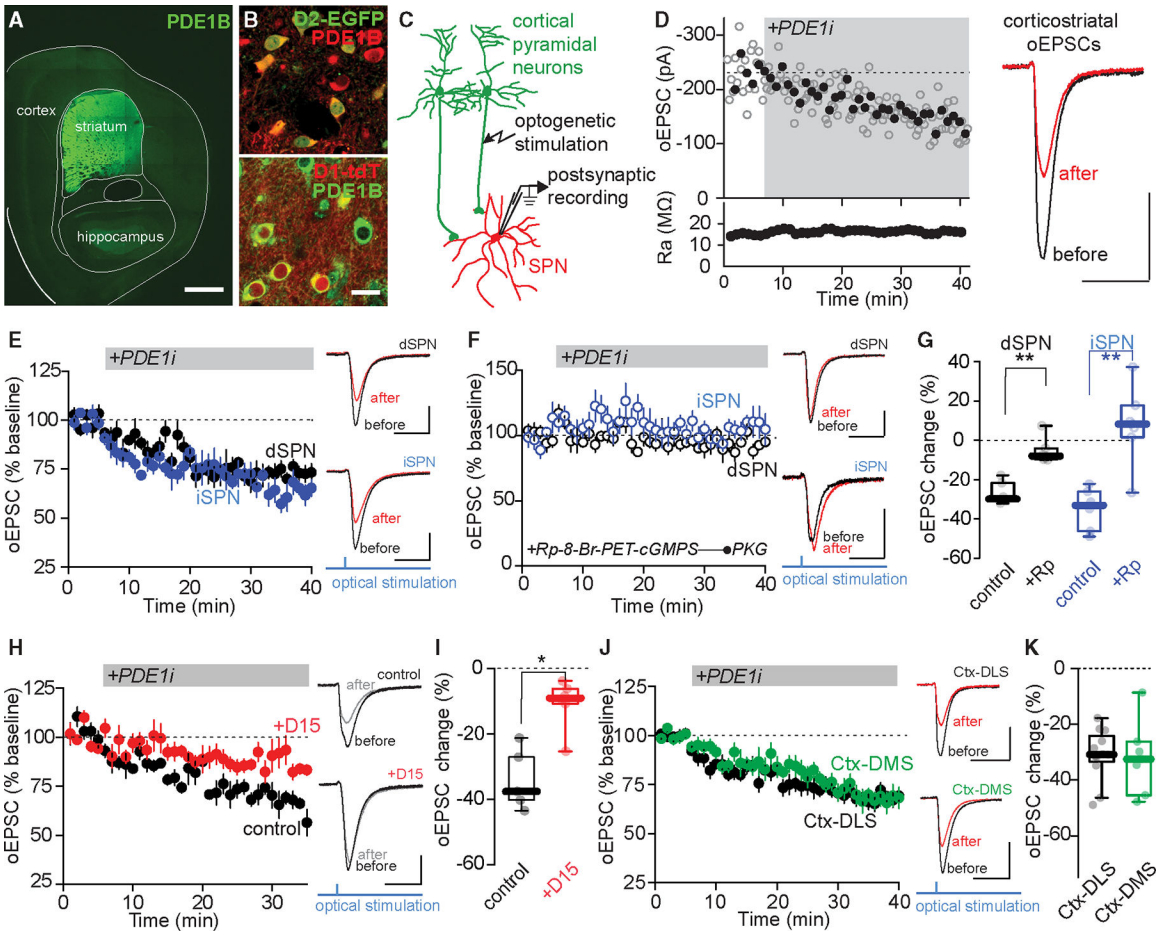

Figure 1. PDE1 inhibition led to cGMP-dependent LTD at corticostriatal synapses in SPNs

(A) Composite confocal image showing strong expression of PDE1B in the striatum. Scale bar, 1 mm.

(B) Confocal images showing colocalization of PDE1B immunoreactivity with D2-EGFP fluorescence (top) and D1-tdTomato (tdT) fluorescence (bottom). Scale bar, 20 μm.

(C) Schematic diagram of the recording configuration. Whole-cell patch-clamp recordings were made from SPNs in acute brain slices of Thy1-ChR2 mice, and EPSCs were optogenetically evoked with brief blue LED pulses.

(D) Sample whole-cell recording from an SPN upon bath application of specific PDE1 inhibitor AF64196 (PDE1i, 0.28 μM). Plots show amplitudes of oEPSC and access resistance (Ra) as a function of time. The filled symbols specify the averages of six data points. The dashed line represents the average EPSC amplitude before PDE1i application. The averaged EPSC traces before and 30 min after PDE1 inhibition are shown on the right. Here and in (E), (F), (H), and (J), scale bars represent 100 pA × 20 ms.

(E) Left, application of PDE1i-induced synaptic depression in the SPNs of the direct and indirect pathways. Time course of normalized EPSC in dSPNs (black, $n = 6$ neurons from 5 animals) and iSPNs (blue, $n = 6$ neurons from 5 animals) upon bath application of PDE1i is shown. Data are represented as mean ± SEM. Right, sample EPSC traces before and 30 min after PDE1 inhibition.

Author Manuscript Author Manuscript Author Manuscript Author Manuscript

(F) Left, intracellular dialysis of PKG inhibitor Rp-8-Br-PET-cGMPS (Rp, 10 mM) blocked PDE1i-induced LTD in both dSPNs (black, $n = 6$ neurons from 3 animals) and iSPNs (blue, $n = 7$ neurons from 4 animals).

(G) Boxplot summary of data in (E) and (F) showing changes in oEPSC (relative to baseline) from the last 5 min of recordings. $^{**}p < 0.01$; Mann-Whitney test.

(H) Left, endocytosis-disrupting peptide D15 (1 mM), when applied intracellularly, impairs PDE1i-LTD ($n = 6$).

(I) Boxplot summary of changes in oEPSC caused by PDE1i in the presence of intracellular D15 peptide and in interleaved controls. $^{*}p < 0.05$; Mann-Whitney test.

(J) Left, PDE1i induces similar synaptic depression of EPSC at cortex (Ctx)-DLS synapses ($n = 12$ neurons from 10 animals) and Ctx-DMS synapses ($n = 7$ neurons from 5 animals). Right, sample EPSC traces before and 30 min after PDE1 inhibition.

(K) Boxplot summary of data in (J) showing changes in oEPSC from the last 5 min of recordings.

Author Manuscript Author Manuscript Author Manuscript Author Manuscript

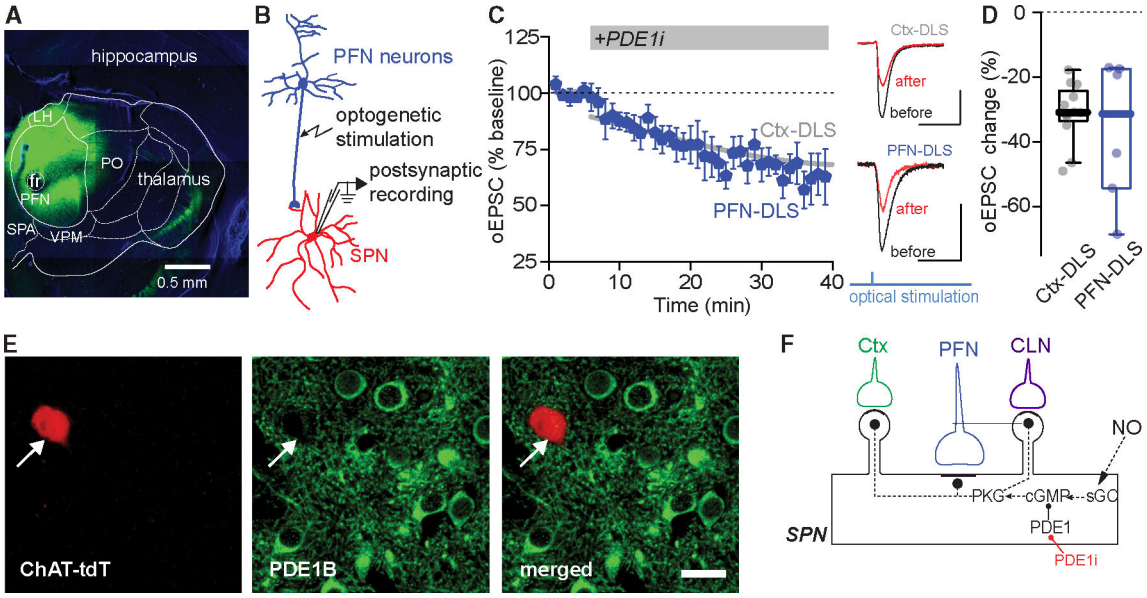

Figure 2. PDE1 inhibition led to LTD at thalamostriatal synapses in SPNs

(A) Representative image of ChR2 expression in the PFN of Grp-KH288 Cre mouse injected with Cre-off ChR2-eYFP. Scale bar, 0.5 mm.

(B) Schematic diagram of the recording configuration. Whole-cell patch-clamp recordings were made from SPNs in acute brain slices of Grp-KH288 Cre mice injected with Cre-off ChR2-eYFP. EPSCs were optogenetically evoked with brief blue LED pulses.

(C) Left, PDE1i induces similar depression of EPSC at PFN-DLS synapses ($n = 6$ neurons from 4 animals) and Ctx-DLS synapses (fitted line, $n = 12$ neurons from 10 animals). Data are represented as mean ± SEM. Right, sample EPSC traces before and 30 min after PDE1 inhibition. Scale bars are 100 pA × 20 ms.

(D) Boxplot summary of data in (C) showing changes in oEPSC from the last 5 min of recordings.

(E) Representative confocal images showing lack of PDE1B immunoreactivity in ChIs labeled by tdTomato fluorescence (ChAT-tdT) in ChAT-Cre × Ai14 mice. Scale bar, 20 μm.

(F) Schematic showing the modulation of NO-cGMP signaling in SPNs by PDE1i and downstream effect at corticostriatal and thalamostriatal synapses. CLN, centrolateral nucleus of the thalamus.

Author Manuscript Author Manuscript Author Manuscript Author Manuscript

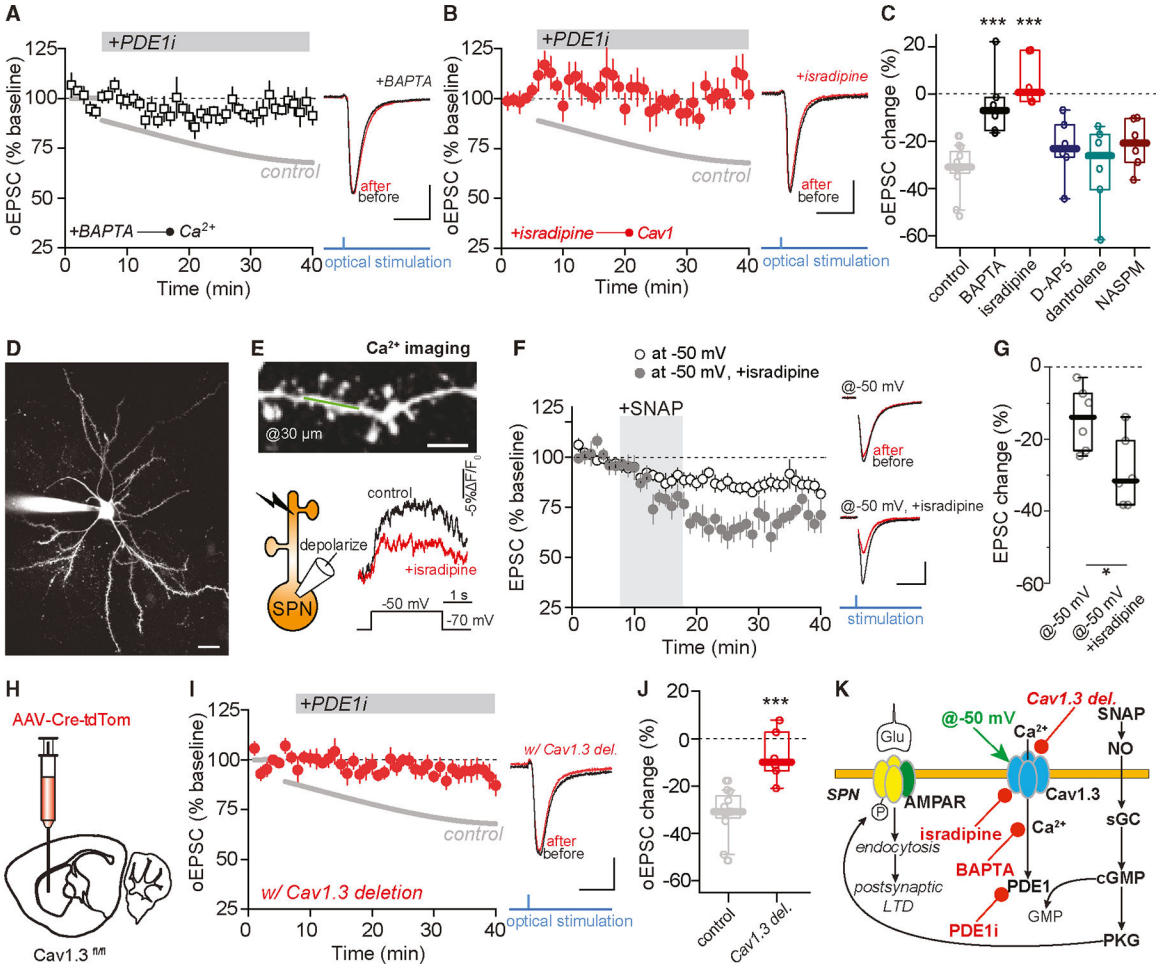

Figure 3. PDE1 activity depends on $Ca_V1.3$ Ca^{2+} channels

(A) PDE1i-LTD is blocked by intracellular BAPTA (5 mM, $n = 6$ neurons from 4 animals). Fitted historical control ($n = 12$ neurons from 10 animals) was shown as a gray line. Here and in (B), (F), and (I), data are represented as mean ± SEM. Sample EPSC traces before PDE1i application and from the last 5 min of recording are shown on the right. Here and in (B), (F), and (I), scale bars represent 100 pA × 20 ms.

(B) PDE1i-LTD is blocked by isradipine, a negative allosteric modulator of Ca_V1 calcium channels (2 µM, $n = 6$ neurons from 4 animals).

(C) Boxplot summary of changes in oEPSC (relative to baseline) induced by PDE1i application in the presence of various inhibitors. ***$p < 0.001$ compared to control; Mann-Whitney test. See also Figure S4.

(D) Two-photon image of an SPN dialyzed with Fluo-4 and Alexa Fluor 568 through the patch pipette. Scale bar, 20 µm.

(E) Top, two-photon image of a dendritic segment where line scan Ca^{2+} imaging (indicated by a green line) was performed. Scale bar, 5 µm. Bottom left, schematic of dendritic Ca^{2+} imaging. Bottom right, representative Ca^{2+} signals evoked by depolarization from −70 to −50 mV before and after isradipine wash-in (1 µM) aligned with the voltage step protocol. See also Figure S4D.

Author Manuscript Author Manuscript Author Manuscript Author Manuscript

(F) Time course of SNAP-LTD recorded with a holding potential of −50 mV with or without isradipine (−50 mV: $n = 6$ neurons from 6 animals; −50 mV with isradipine; $n = 6$ neurons from 3 animals). Sample EPSC traces are shown on the right.

(G) Boxplot summary of data shown in (F). *$p < 0.05$; **$p < 0.01$; Mann-Whitney test.

(H) Diagram showing injection of Cre recombinase-expressing AAV into the DLS of $Ca_V1.3^{fl/fl}$ mice.

(I) PDE1i-LTD is blocked by genetic knockdown of $Ca_V1.3$ ($n = 6$ neurons from 5 animals).

(J) Boxplot summary of data in (I) showing changes in oEPSC from the last 5 min of recordings. ***$p < 0.001$ compared to control; Mann-Whitney test.

(K) Schematic showing the $Ca_V1.3$-PDE1 signaling pathway that negatively modulates postsynaptic LTD.

Author Manuscript Author Manuscript Author Manuscript Author Manuscript

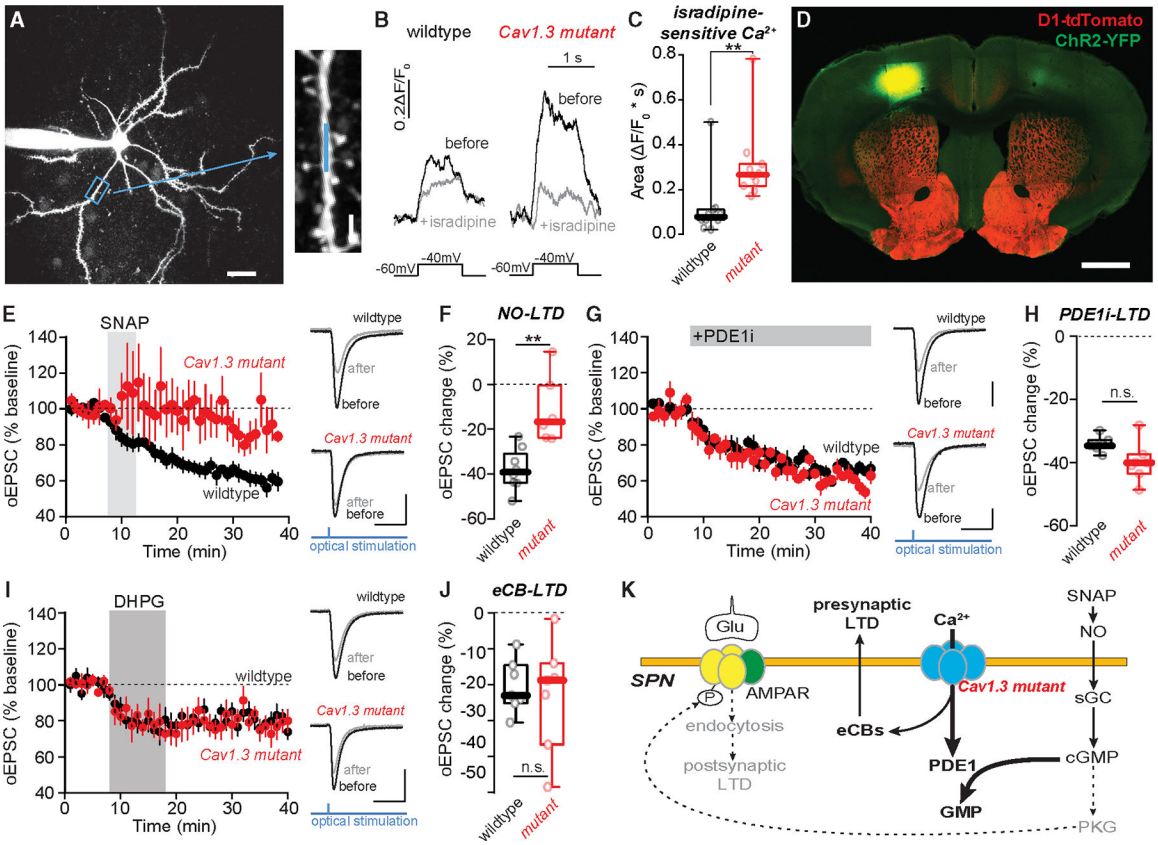

Figure 4. In mice with a G407R mutation in $Ca_V1.3$ channels, abnormal Ca^{2+} signal led to impaired NO-LTD

(A) Schematic depicting the Ca^{2+} imaging assay. Left, a dSPN was patched in the whole-cell configuration, dialyzed with Ca^{2+}-insensitive Alexa Fluor 568 and Ca^{2+}-sensitive Fluo-4. Dendritic Ca^{2+} transients were triggered by somatic depolarization (from −60 to −40 mV for 1 s) through the patch pipette. Two-photon line scan imaging was performed at segments of dendrites ~45 μm from the soma (indicated by the green box). Right, a high-magnification image of a segment of dendrite. Line scan was indicated by the green line. Scale bars, 20 μm (left) and 2 μm (right).

(B) Examples of dendritic Ca^{2+} transients before and after application of isradipine (2 μM) in wild-type siblings or *Cacna1d*$^{G407R/+}$ mice were temporally aligned with the voltage step protocol.

(C) Boxplot summary of isradipine-sensitive component of dendritic Ca^{2+} transient in wild-type and *Cacna1d*$^{G407R/+}$ mice (both $n = 10$ cells from 4 mice). G407R mutation significantly increases depolarization-evoked Ca^{2+} transients in the dendrites. $^{**}p = 0.0011$; Mann-Whitney test.

(D) Representative confocal image of ChR2 expression in the motor cortex of D1-tdTomato mouse. Scale bar, 1 mm.

(E) NO-LTD is impaired in *Cacna1d*$^{G407R/+}$ mice. EPSC was evoked by wide-field blue LED illumination (0.3 ms). LTD was induced by bath application of SNAP (5 μM) for 5 min (indicated by the gray vertical bar). Plot shows EPSC amplitude as a function of time.

Author Manuscript Author Manuscript Author Manuscript Author Manuscript

Data are mean ± SEM. n = 8 dSPNs from 6 wild-type mice and n = 6 dSPNs from 4 *Cacna1d*$^{G407R/+}$ mice. Scale bars in (E), (G), and (I) represent 200 pA × 20 ms.

(F) Boxplot summary of LTD amplitudes from the last 10 min of recordings shown in (E). In *Cacna1d*$^{G407R/+}$ mice, SNAP-induced LTD was significantly impaired. **p < 0.01; Mann-Whitney test.

(G) PDE1i-LTD is normal in *Cacna1d*$^{G407R/+}$ mice. Plot shows EPSC amplitudes as a function of time. Data are mean ± SEM. Both n = 7 neurons from 4 animals.

(H) Boxplot summary of PDE1i-LTD recordings shown in (G). PDE1i induced similar synaptic depression at corticostriatal glutamatergic synapses in *Cacna1d*$^{G407R/+}$ mice and interleaved wild-type littermates. n.s., not statistically significant; Mann-Whitney test.

(I) eCB-LTD is similar in wild-type and *Cacna1d*$^{G407R/+}$ mice. Here, eCB-LTD was induced by DHPG (50 μM) application for 10 min (indicated by the gray vertical bar) at a holding potential of −60 mV in the presence of 1.2 mM Ca^{2+} in the bath solution. Data are mean ± SEM. Both n = 7 dSPNs from 5 mice. See also Figure S6.

(J) Boxplot summary of LTD amplitudes from the last 10 min of recordings shown in (I). The near-threshold eCB-LTD protocol induced similar synaptic depression in wild-type and *Cacna1d*$^{G407R/+}$ mice. Mann-Whitney test.

(K) Schematic showing that abnormal activity of the $Ca_V1.3$-PDE1 signaling pathway in the SPNs of *Cacna1d*$^{G407R/+}$ mice impairs postsynaptic LTD.

Author Manuscript Author Manuscript Author Manuscript Author Manuscript

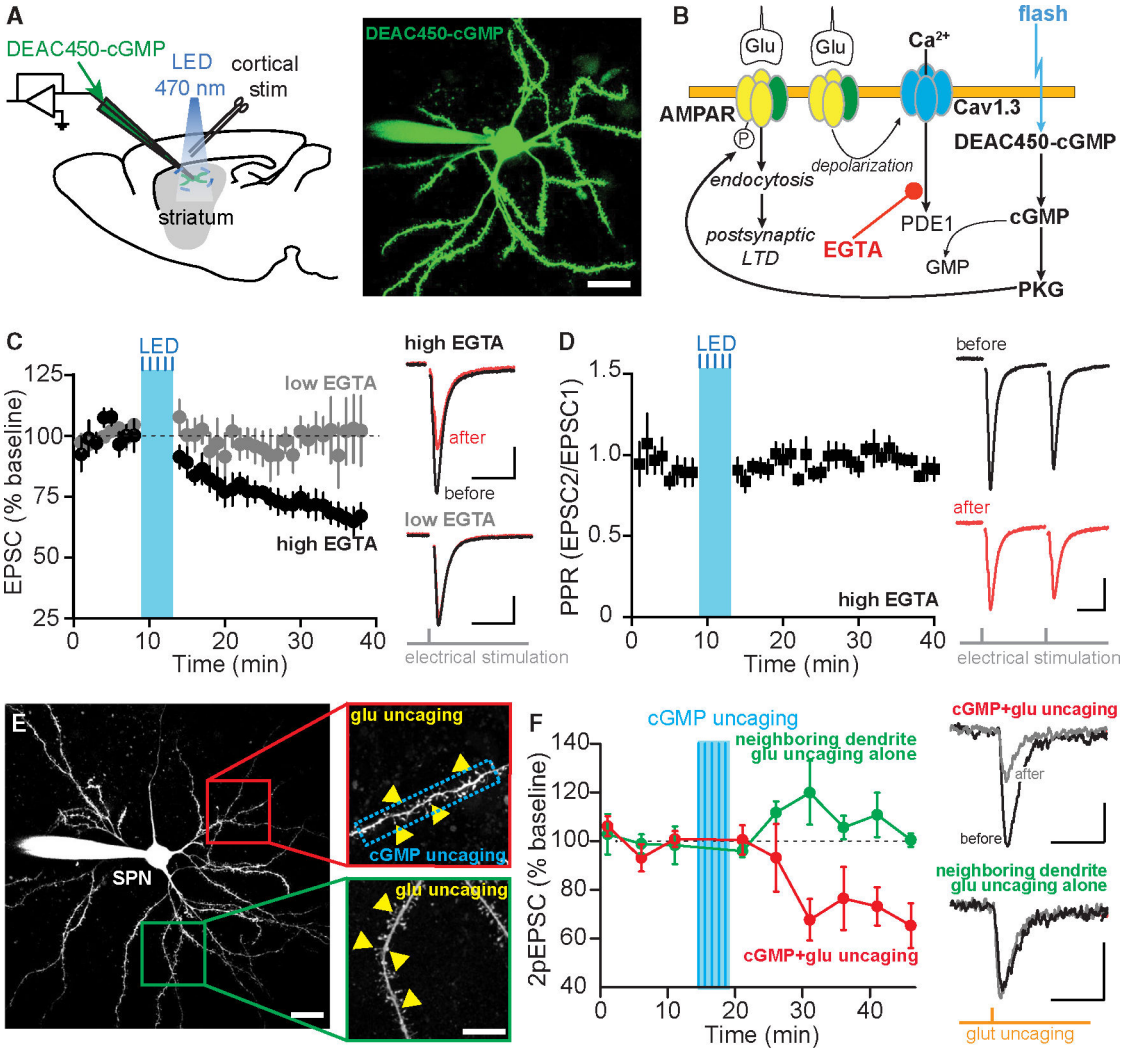

Figure 5. NO/cGMP-induced LTD is negatively regulated by intracellular Ca^{2+}

(A) Left, schematic of experimental configuration for intracellular cGMP uncaging. Right, two-photon image of an SPN filled with caged cGMP (DEAC450-cGMP) through the patch pipette. Scale bar, 20 μm.

(B) Schematic showing that induction of postsynaptic LTD by cGMP uncaging is permitted only when intracellular Ca^{2+} is dampened by high EGTA concentration.

(C) Time course of electrically evoked EPSC before and after wide-field illumination with 470-nm LED (200 ms every minute, repeated 5 times) in SPNs intracellularly filled with DEAC450-cGMP (75 μM) supplemented with 5 mM EGTA (“high EGTA”; $n = 7$ neurons from 6 mice) or 0.25 mM EGTA (“low EGTA”; $n = 6$ neurons from 5 mice). In (C) and (D), data are mean ± SEM, and scale bars represent 100 pA × 20 ms.

(D) Time course of PPR of EPSC in the SPNs with high EGTA (the same cells as in C).

(E) Experimental design of dual-color uncaging. Two-photon fluorescence images of an SPN (left) and its dendritic segments (right) are shown. SPNs were filled with 50 μM Alexa Fluor 594 and 75 μM DEAC450-cGMP supplemented with 5 mM EGTA. The synaptic strengths of dendritic spines were assayed by glutamate (glu) uncaging with 1-ms pulses of

Author Manuscript Author Manuscript Author Manuscript Author Manuscript

720-nm two-photon laser (yellow triangles). cGMP uncaging was performed either on the same dendrite (upper right) with a 473-nm laser that covered a ~35-μm dendritic segment (blue rectangle) or on a different dendrite (lower right). Scale bars, 20 μm (left) and 10 μm (right).

(F) Left, plot of normalized two-photon glutamate uncaging-evoked EPSCs (2pEPSCs) as a function of time with localized cGMP uncaging on the same dendrite (n = 5 neurons from 3 animals) or a different dendrite (n = 4 neurons from 3 animals). Right, representative traces of 2pEPSCs before (black) and 20 min after (gray) cGMP uncaging in the same dendrite or in a different dendrite. Data are mean ± SEM. Scale bars, 10 pA × 50 ms.

Author Manuscript Author Manuscript Author Manuscript Author Manuscript

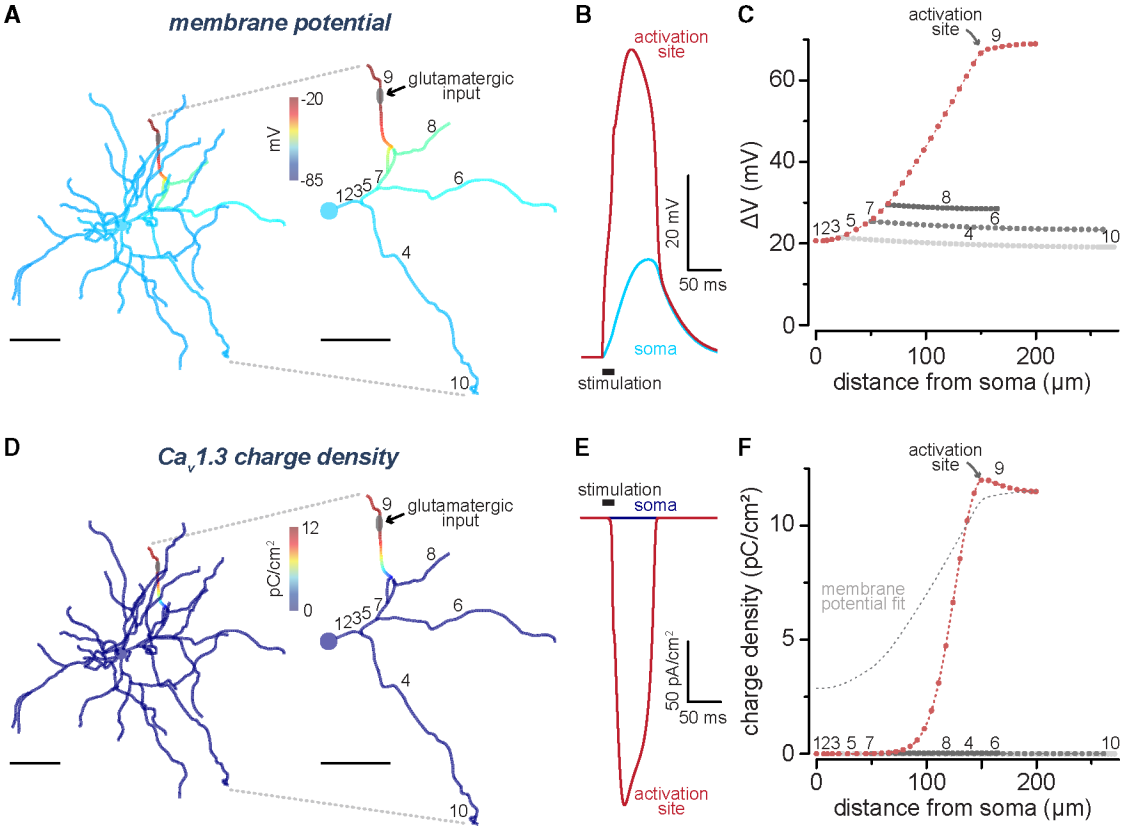

Figure 6. Computational modeling revealed dendritic compartmentalization of membrane depolarization and $Ca_V1.3$ activation in response to dendritic spike generation

(A) Two-dimensional heatmap of a morphologically reconstructed dSPN illustrates peak membrane potential within the entire dendritic arbor in response to a dendritic spike. A dendritic spike is simulated at a distal location, as indicated by the arrow, by suprathreshold glutamatergic input (i.e., stimulating 18 neighboring synapses sequentially at 1-ms intervals in the distal-to-proximal direction). The magnified section shows peak membrane potential within the dendritic path from the activation site to soma and in any major dendritic branches arising from this path (dendritic segments labeled 1–10). Scale bars here and in (D), 50 μm.

(B) Simulated synaptic potentials generated by clustered input at the site of activation and at the soma.

(C) Peak change in membrane potential plotted as a function of path distance to the center of the soma for dendritic tree illustrated in the magnified section of (A).

(D) Equivalent two-dimensional heatmap and magnified section show total charge density (pC/cm^2) due to activation of $Ca_V1.3$.

(E) Local current density (pA/cm^2) of $Ca_V1.3$ at the dendritic site of activation and soma. Charge density was calculated as the area under the current density plots over time.

(F) Peak change in charge density plotted as a function of path length to the center of the soma at the same locations as in (C). The fitted line showing membrane potential change along the main path from (C) has been superimposed to demonstrate the additional tuning effect the voltage-gating properties of $Ca_V1.3$ has on the spatial profile of charge density within the dendritic tree. Data in (C) and (F) were fitted using univariate smoothing splines.

Author Manuscript Author Manuscript Author Manuscript Author Manuscript

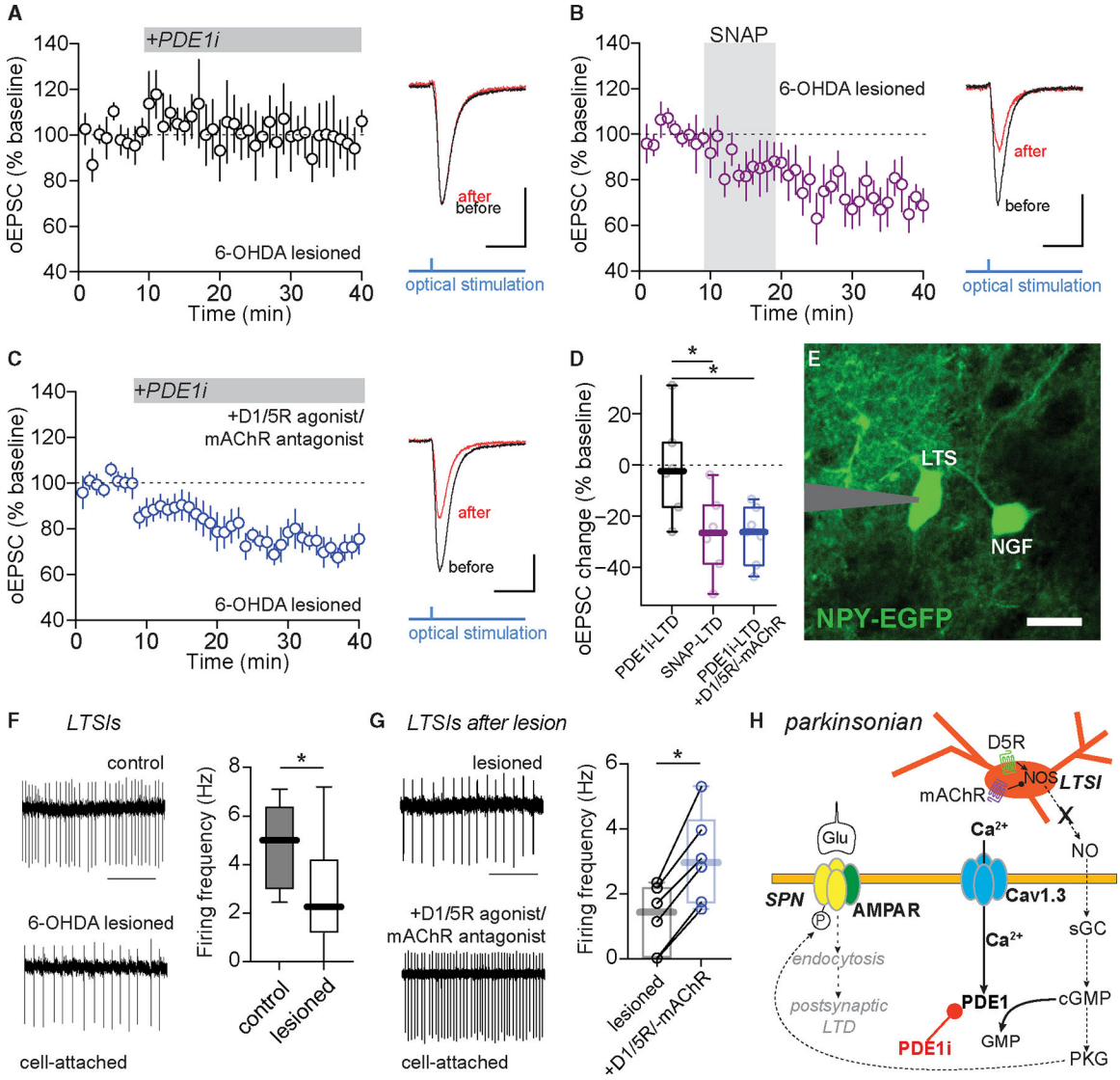

Figure 7. Endogenous NO release by LTSIs was impaired in parkinsonian mice and rescued by restoring the DA-ACh balance

(A) PDE1 inhibition fails to induce synaptic depression at corticostriatal synapses in iSPNs of 6-OHDA-lesioned mice ($n = 6$ neurons from 3 mice). In (A)–(C), time course data represented as mean ± SEM are shown on the left. Sample EPSC traces before PDE1i application and from the last 5 min of recording are shown on the right. Scale bars, 100 pA × 20 ms.

(B) SNAP-LTD is intact in iSPNs of 6-OHDA-lesioned mice ($n = 6$ neurons from 4 mice).

(C) In the presence of D1R/D5R-type agonist SKF 81297 (3 μM) and mAChR antagonist scopolamine (10 μM), PDE1i-LTD is restored ($n = 7$ neurons from 4 mice).

(D) Boxplot summary of data in (A)–(C) showing changes in oEPSC from the last 5 min of recordings. *$p < 0.05$; Mann-Whitney test.

(E) Two-photon image of a LTSI in slices from NPY-EGFP mice recorded in cell-attached mode. Scale bar, 20 μm.

Author Manuscript Author Manuscript Author Manuscript Author Manuscript

(F) Left, examples of cell-attached recordings from LTSIs in slices from control or 6-OHDA-lesioned NPY-EGFP mice. Scale bars in (F) and (G) represent 2 s. Right, boxplot summary of firing rates of LTSIs (control, $n = 7$ neurons from 3 mice; 6-OHDA lesioned, $n = 18$ neurons from 4 mice). $*p < 0.05$; Mann-Whitney test.

(G) Left, examples of cell-attached recordings from LTSIs from 6-OHDA-lesioned NPY-EGFP mice before and after application of SKF 81297 and scopolamine ($n = 6$ neurons from 3 mice). Right, boxplot summary of LTSI firing frequency in lesioned mice before and after application of D1-type agonist and mAChR antagonist. $*p < 0.05$; Wilcoxon test.

(H) Schematic showing that in parkinsonian mice, lack of D5R signaling and enhanced mAChR signaling led to reduction in endogenous NO release and postsynaptic LTD.

Author Manuscript Author Manuscript Author Manuscript Author Manuscript

KEY RESOURCES TABLE

REAGENT or RESOURCE	SOURCE	IDENTIFIER
Antibodies		
Rabbit monoclonal anti-PDEIB antibody	Abcam	Cat#ab182565
Goat anti-rabbit secondary antibody Alexa Fluor 488	nvitrogen	Cat#A-11008; RRID:AB_143165
Goat anti-rabbit secondary antibody Alexa Fluor 555	nvitrogen	Cat#A-21428; RRID:AB_2535849
Rabbit anti-GAPDH monoclonal antibody	Cell Signaling	Cat#2118; RRID:AB_561053
Horseradish peroxidase-conjugated anti-rabbit secondary antibody	Cell Signaling	Cat#7074; RRID:AB_2099233
Bacterial and virus strains		
AAV5-hSyn-hChR2(H134R)-EYFP	Addgene (a gift from Karl Deisseroth)	Plasmid # 26973; http://n2t.net/addgene:26973; RRID:Addgene_26973
AAV9-floxed-cre off-hEF1a-ChR2-EYFP-WRE-pA	Virovek, Inc	N/A
AAV9-CMV-Cre-2A-T dtomato	Virovek, Inc	N/A
AAV9-EF1a-DIO-Rpl22L1-myc-FLag-2A-tdTomato	Virovek, Inc	N/A
Chemicals, peptides, and recombinant proteins		
AF64196	Lundbeck; Khammy et al.[44]	N/A
8-MM-IBMX (8-methoxymethyl-3-isobutyl-1-methylxanthine)	Sigma Aldrich	Cat#2547; CAS: 78033-08-6
Rp-8-Br-PET-cGMPS	Tocris	Cat#3028; CAS: 185246-32-6
D15 peptide (Dynamin 828-42)	Stanford Protein and Nucleic Acid Facility; Shupliakov et al.[45]	N/A
Mecamylamine hydrochloride	Tocris	Cat# 2843; CAS: 110691-49-1
Scopolamine hydrobromide	Tocris	Cat# 1414; CAS: 114-49-8
BAY 60-7550	Cayman Chemical	Cat#10011135, CAS: 439083-90-6
8Br-cGMP (8-Bromo-cGMP)	Tocris	Cat#1089; CAS: 51116-01-9
Fura-2, pentapotassium salt, cell impermeant	Thermo Fisher Scientific	Cat#F-1200
Fluo-4, pentapotassium salt, cell impermeant	Thermo Fisher Scientific	Cat#F-14200
Alexa Fluor 568 hydrazide	Thermo Fisher Scientific	Cat#A-10437
BAPTA	Thermo Fisher Scientific	Cat#B1204; CAS: 85233-19-8
Isradipine	Tocris	Cat#2004; CAS: 75695-93-1
D-AP5	Tocris	Cat#0106; CAS: 79055-68-8
Dantrolene, sodium salt	Tocris	Cat#0507; CAS: 14663-23-1
NASPM trihydrochloride	Tocris	Cat#2766; CAS: 1049731-36-3
SNAP	Tocris	Cat#0598; CAS: 79032-48-7
DHPG ((S)-3,5-DHPG)	Tocris	Cat#0805; CAS: 162870-29-3
DEAC450-cGMP	Laboratory of Graham Ellis-Davies; Agarwal et al.[52]	N/A
EGTA	Tocris	Cat#2807; CAS: 67-42-5
MNI-glutamate	Tocris	Cat#1490; CAS: 295325-62-1
6-OHDA (6-hydroxydopamine hydrochloride	Sigma Aldrich	Cat#H4381; CAS: 28094-15-7

Author Manuscript Author Manuscript Author Manuscript Author Manuscript

REAGENT or RESOURCE	SOURCE	IDENTIFIER
SKF 81297	Sigma Aldrich	Cat#S143; CAS: 71636-61-8
Picrotoxin	Tocris	Cat#1128; CAS: 124-87-8
Critical commercial assays		
RNeasy Micro kit	QIAGEN	Cat#74004
SuperScript IV VILO (SSIV VILO) Master Mix	Thermo Fisher Scientific	Cat#11756500
TaqMan PreAmp Master Mix	Thermo Fisher Scientific	Cat#4391128
TaqMan Fast Advanced Master Mix	Thermo Fisher Scientific	Cat#4444557
Deposited data		
NEURON + Python model of a reconstructed SPN	This paper	Zenodo: https://doi.org/10.5281/zenodo.12213216
Experimental models: Organisms/strains		
Mouse: B6.Cg-Tg(Thy1-COP4/EYFP) 18Gfng/J (Thy1-ChR2-YFP)	The Jackson Laboratory	RRID:IMSR_JAX:007612
Mouse: FVB.Cg-Tg(Drd1-tdTomato) 5Calak, C57BL/6 background	Laboratory of Nicole Calakos	RRID: MMRRC_030512-UNC
Mouse: Tg(Drd2-EGFP)S118Gsat/Mmnc, C57BL/6 background	GENSAT	RRID: MMRRC_000230-UNC
Mouse: Cacna1d$^{G407R/+}$	Laboratory of Anis Contractor; this paper	N/A
Mouse: Tg(Grp-cre)KH288Gsat/Mmucd	MMRRC	RRID:MMRRC_031183_UCD
Mouse: B6; 129S6-Chat$^{tm2(cre)Lowl}$/J	The Jackson Laboratory	RRID:IMSR_JAX:006410
Mouse: B6; 129S6-Gt(ROSA) 26Sortm14(CAG-tdTomato)Hze/J	The Jackson Laboratory	RRID:IMSR_JAX:007908
Mouse: $Ca_V1.3^{fL/fL}$	Laboratory of Paul T. Schumacker; this paper	N/A
Mouse: B6.FVB-Tg(Npy-hrGFP)1Lowl/J	The Jackson Laboratory	RRID:IMSR_JAX:006417
Oligonucleotides		
Probe for HPRT	Thermo Fisher Scientific	ID: Mm03024075_m1
Probe for $Ca_V1.2$	Thermo Fisher Scientific	ID: Mm01188822_m1
Probe for $Ca_V3.1$	Thermo Fisher Scientific	ID: Mm00486549_m1
Upper primer for $Ca_V1.3$: CCTGATTATTTTTACAGTGGAG	This paper	N/A
Lower primer for $Ca_V1.3$: TCCATTCCTAACGTAAGCAT	This paper	N/A
Probe for $Ca_V1.3$: ATAGCGTATGGACTGTTGCTG	This paper	N/A
Software and algorithms		
Prairie View 5.3	Bruker	RRID:SCR_017142
Clampfit 10.5	Molecular Devices	RRID:SCR_011323
Origin 8 or 2020	Origin Lab	RRID:SCR_014212
Prism 6 or 9	GraphPad	RRID:SCR_002798
ImageJ	NIH	RRID:SCR_003070

Author Manuscript Author Manuscript Author Manuscript Author Manuscript

REAGENT or RESOURCE	SOURCE	IDENTIFIER
Python 3.9.16	Python programming language	www.python.org; RRID:SCR_008394
Neuron 8.2	The NEURON simulator	https://nrn.readthedocs.io/en/8.2.4/; RRID:SCR_005393
Other		
Vibratome	Leica Biosystems	VT1200S
LED light	CoolLED	pE-100-470
Two-photon laser scanning microscope	Bruker	Ultima
Syringe pump	World Precision Instruments	SP100i
Two-photon excitation laser for imaging	Coherent	Chameleon Ultra I
Two-photon excitation laser for uncaging	Coherent	Mira 900F/Verdi 8W
Photomultiplier tube (PMT, 580-620 nm)	Hamamatsu Photonics	R3982
GaAsP PMT (490-560 nm)	Hamamatsu Photonics	H7422P-40
473 nm laser beam	Prairie Technologies	Aurora
Stereotaxic frame	David Kopf Instruments	Model 940
Confocal laser scanning microscope	Olympus	FV10i